Supporting Information for

Tuning the structure and solubility of nanojars by peripheral ligand substitution, leading to unprecedented liquid-liquid extraction of the carbonate ion from water into aliphatic solvents

Basil M. Ahmed, Brice Calco and Gellert Mezei*

Department of Chemistry, Western Michigan University, Kalamazoo, Michigan, USA

*Correspondent author. Email: gellert.mezei@wmich.edu

CONTENTS **PAGE**

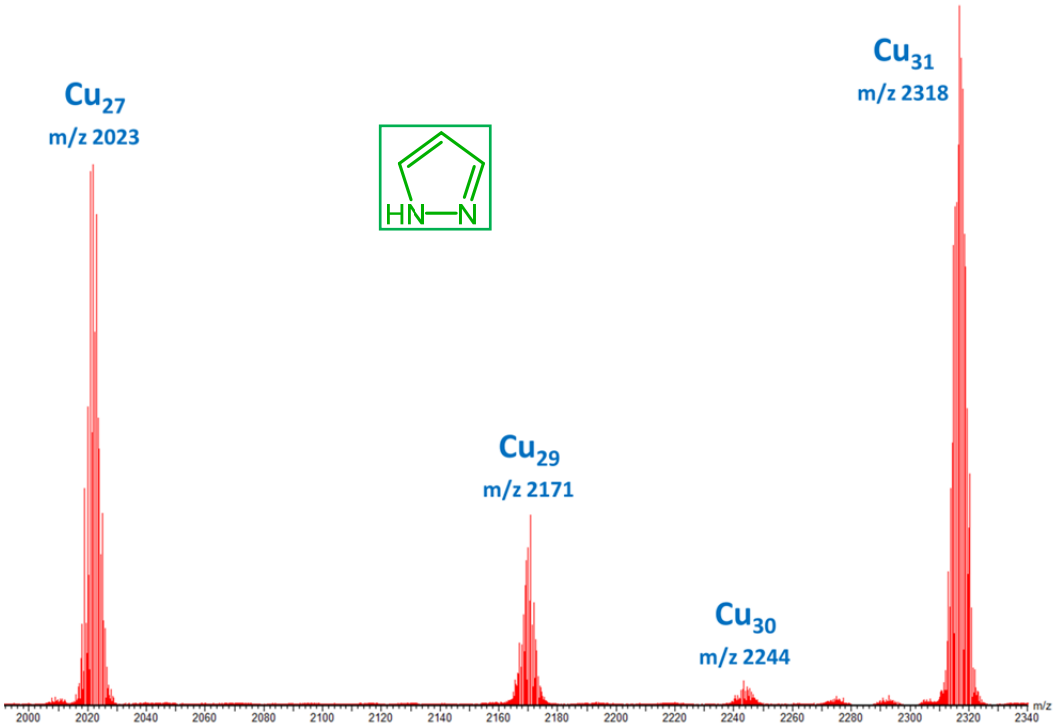

Figure S1. ESI-MS(−) spectrum of $[CO_3 \subset \{Cu(OH)(Hpz)\}_n]^{2-}$ (n = 27, 29, 30, 31).

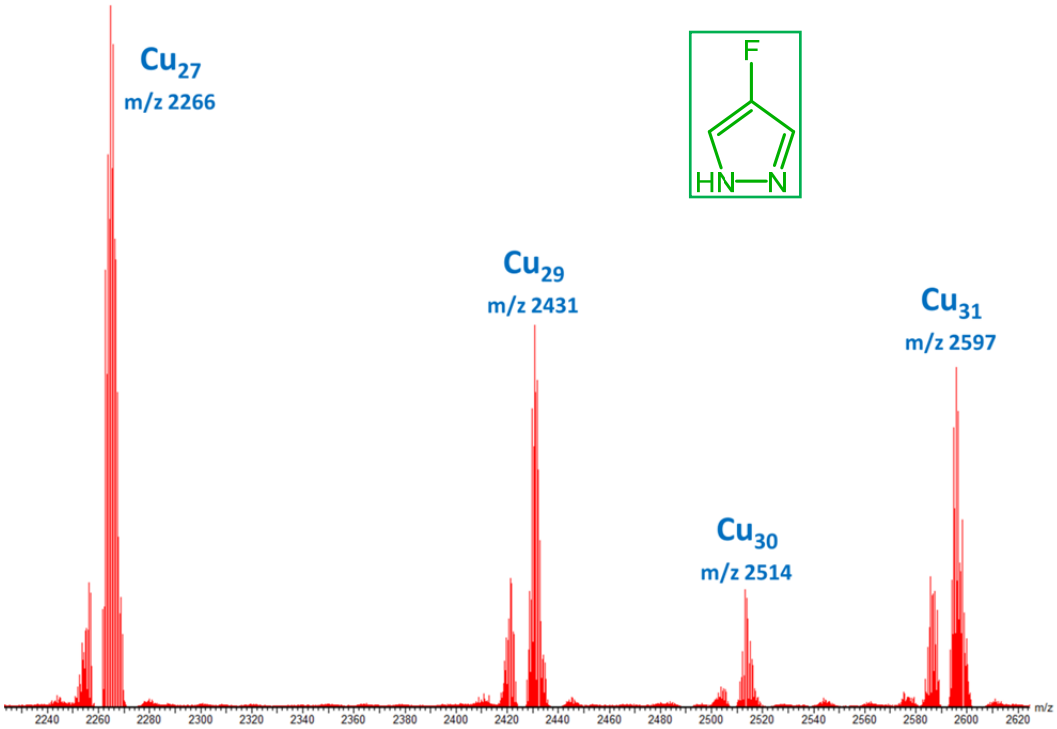

Figure S2. ESI-MS(−) spectrum of $[CO_3 \subset \{Cu(OH)(4\text{-}Fpz)\}_n]^{2-}$ (n = 27, 29, 30, 31).

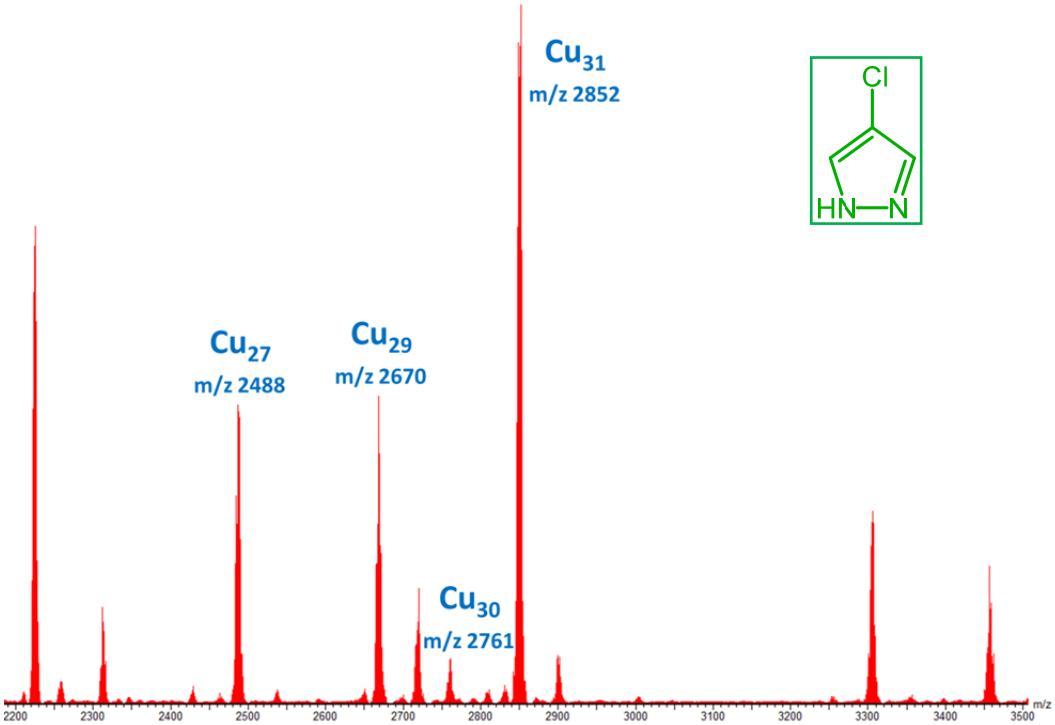

Figure S3. ESI-MS(−) spectrum of $[CO_3 \subset \{Cu(OH)(4\text{-Clpz})\}_n]^{2-}$ (n = 27, 29, 30, 31).

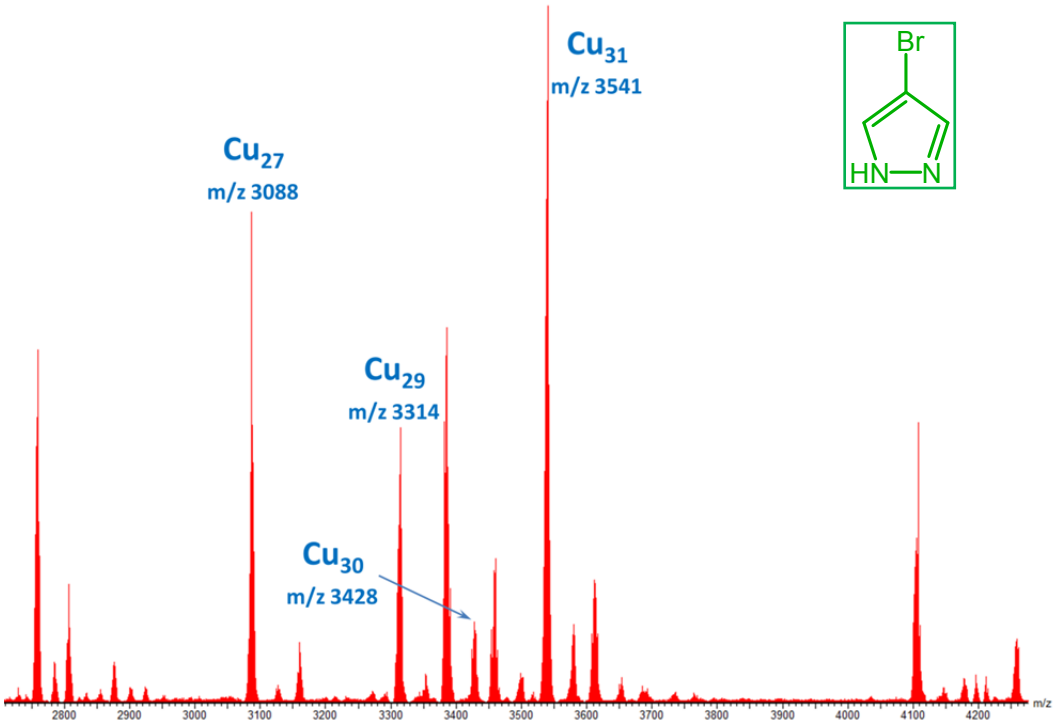

Figure S4. ESI-MS(−) spectrum of $[CO_3 \subset \{Cu(OH)(4\text{-Brpz})\}_n]^{2-}$ (n = 27, 29, 30, 31).

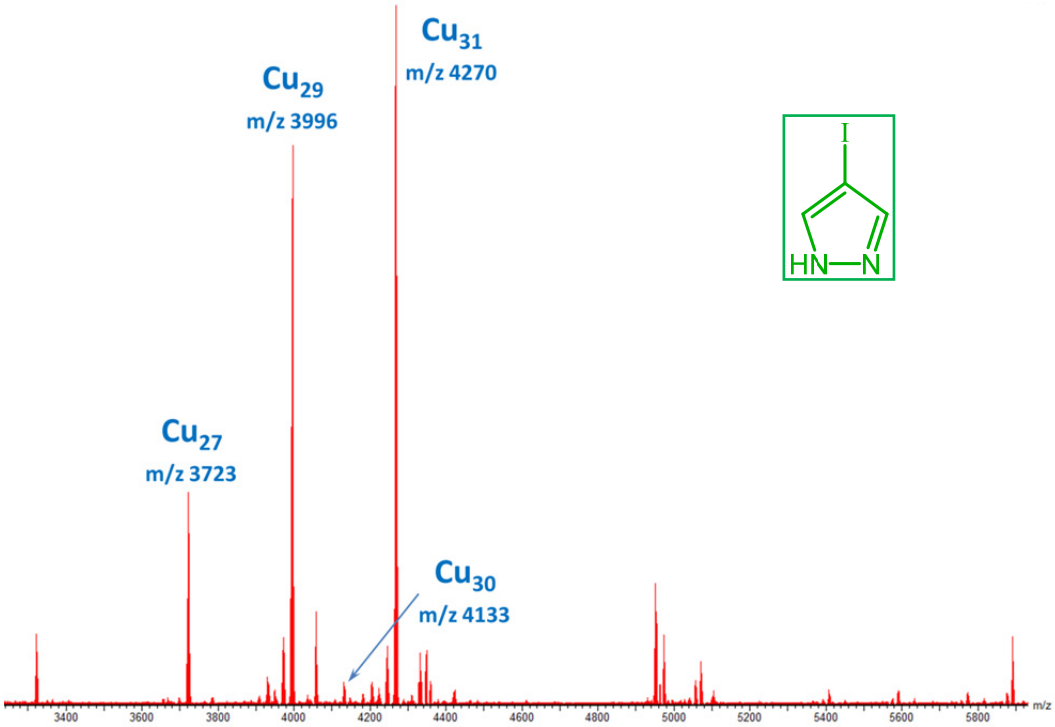

Figure S5. ESI-MS(−) spectrum of $[CO_3 \subset \{Cu(OH)(4\text{-Ipz})\}_n]^{2-}$ (n = 27, 29, 30, 31).

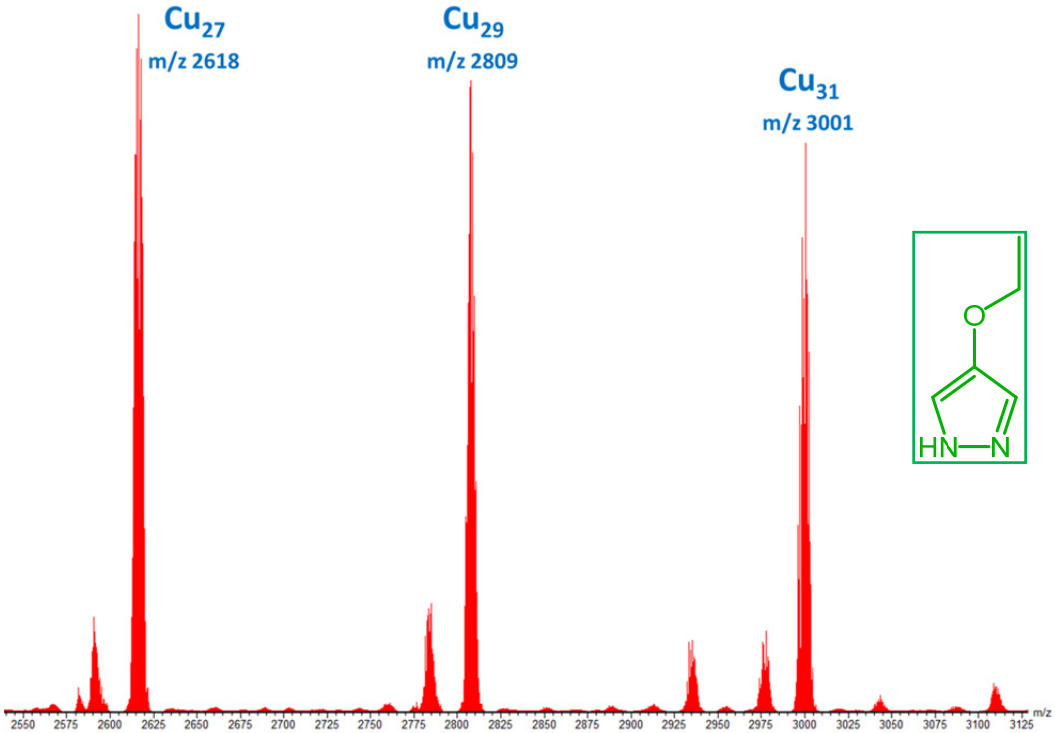

Figure S6. ESI-MS(−) spectrum of $[CO_3 \subset \{Cu(OH)(4\text{-EtOpz})\}_n]^{2-}$ (n = 27, 29, 30, 31).

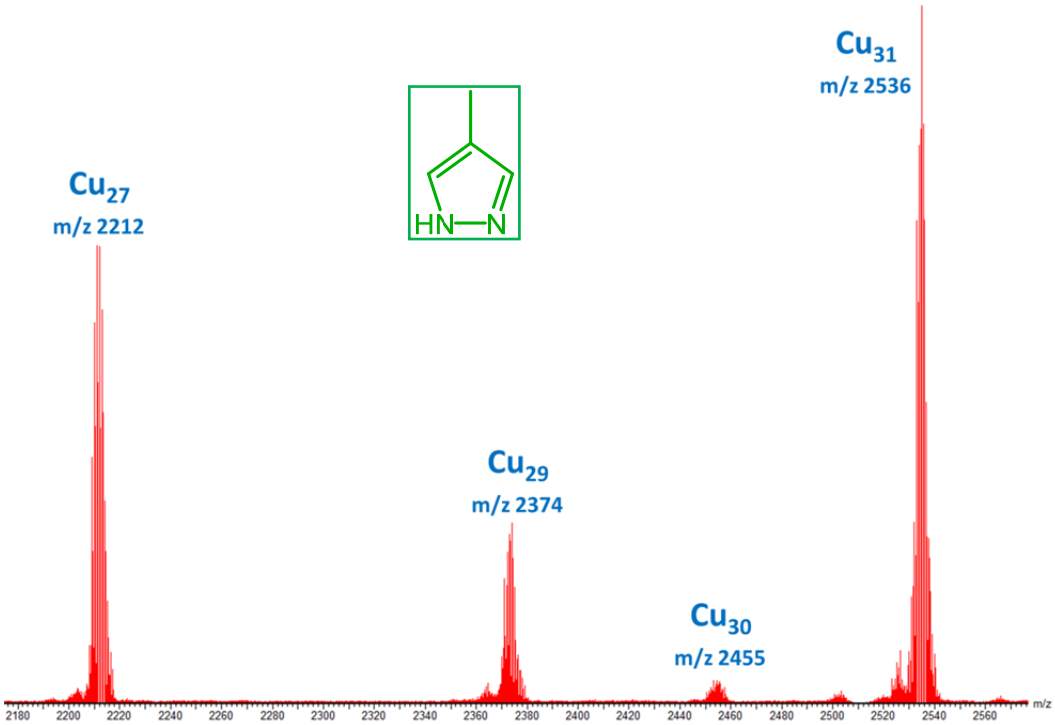

Figure S7. ESI-MS(−) spectrum of $[CO_3 \subset \{Cu(OH)(4\text{-Mepz})\}_n]^{2-}$ (n = 27, 29, 30, 31).

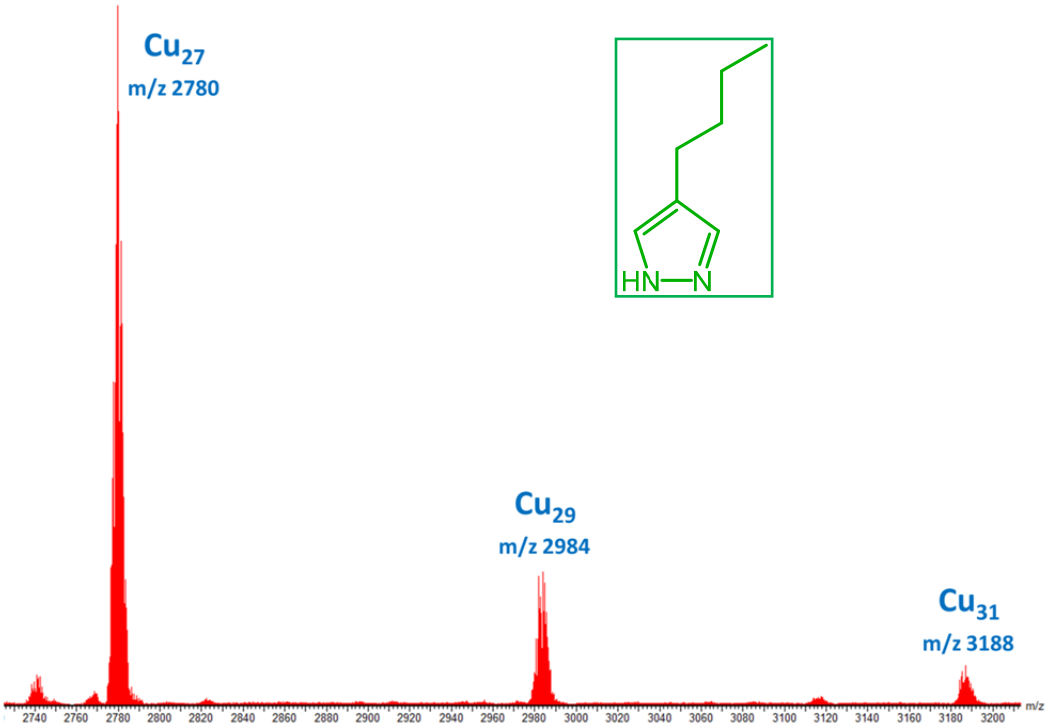

Figure S8. ESI-MS(−) spectrum of $[CO_3 \subset \{Cu(OH)(4\text{-}^{n}\text{Bupz})\}_n]^{2-}$ (n = 27, 29, 31).

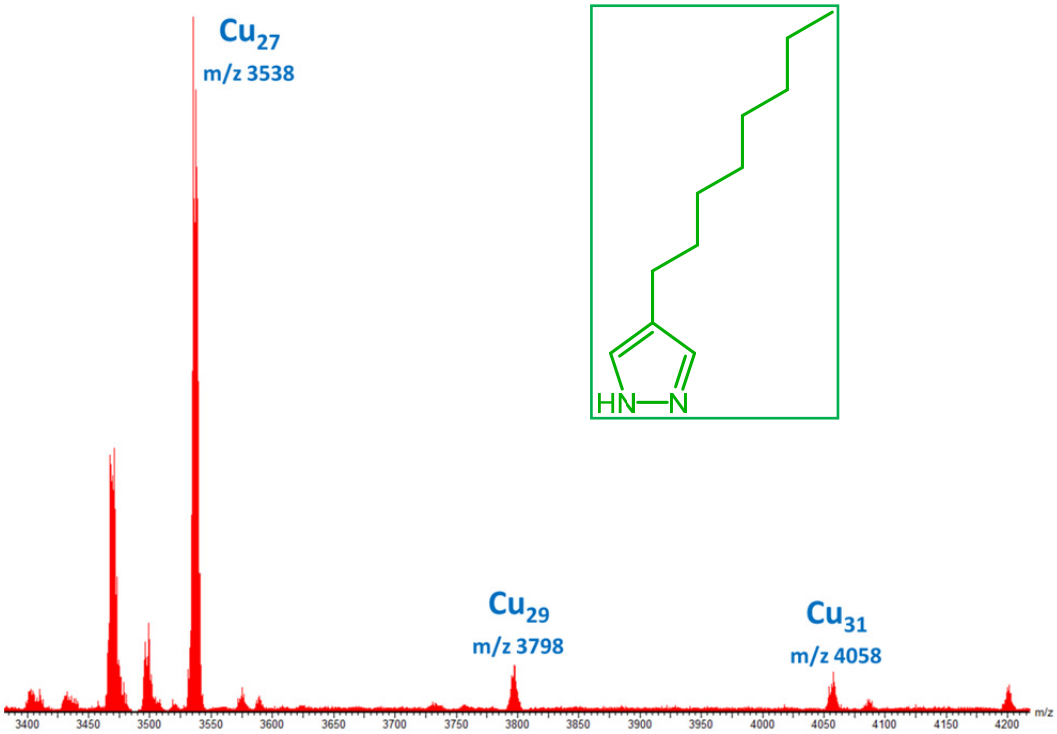

Figure S9. ESI-MS(−) spectrum of $[CO_3 \subset \{Cu(OH)(4\text{-}^{n}Octpz)\}_n]^{2-}$ (n = 27, 29, 31).

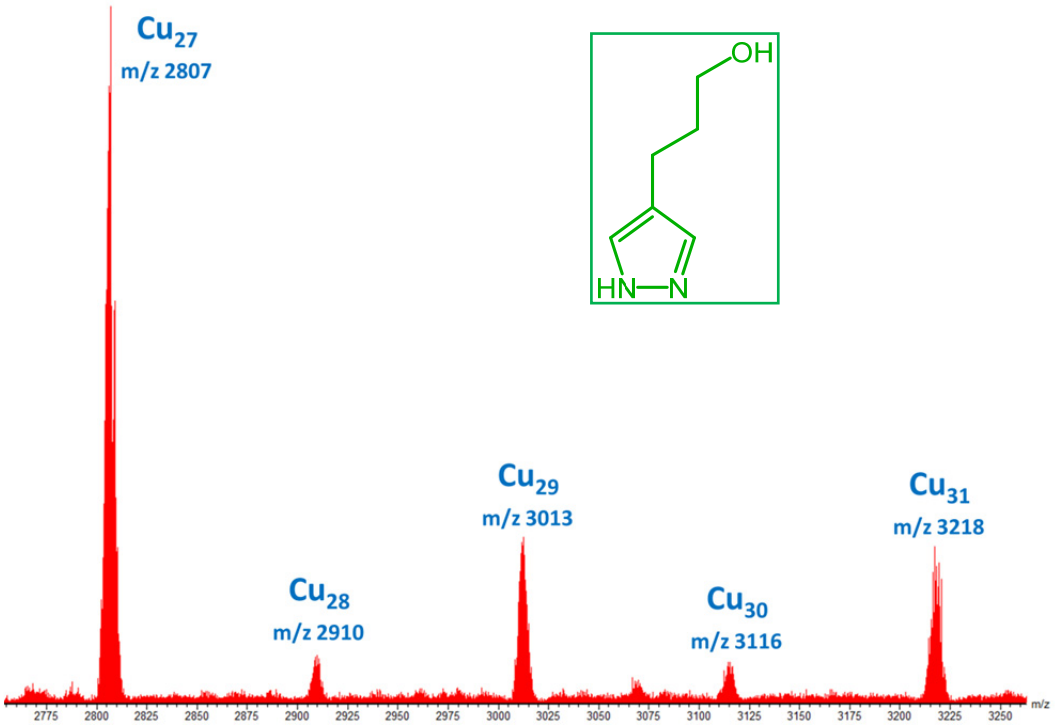

Figure S10. ESI-MS(−) spectrum of $[CO_3 \subset \{Cu(OH)(4\text{-}(HOCH_2CH_2CH_2)pz)\}_n]^{2-}$ (n = 27−31).

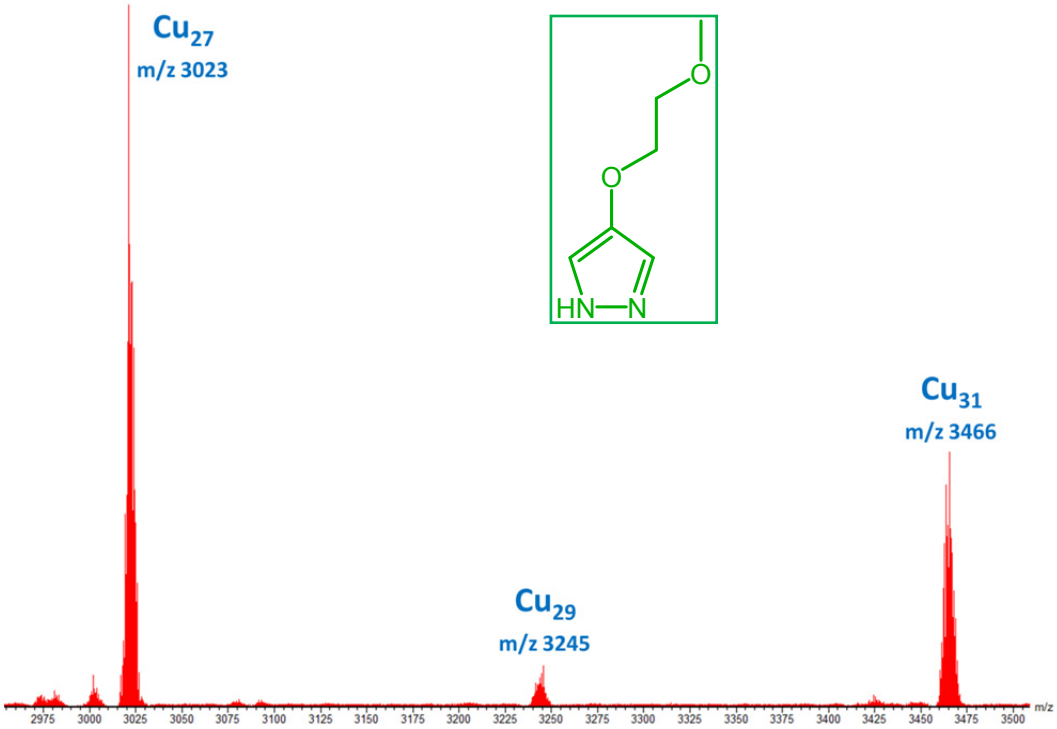

Figure S11. ESI-MS(−) spectrum of $[CO_3 \subset \{Cu(OH)(4\text{-}(CH_3OCH_2CH_2O)pz)\}_n]^{2-}$ (n = 27, 29, 31).

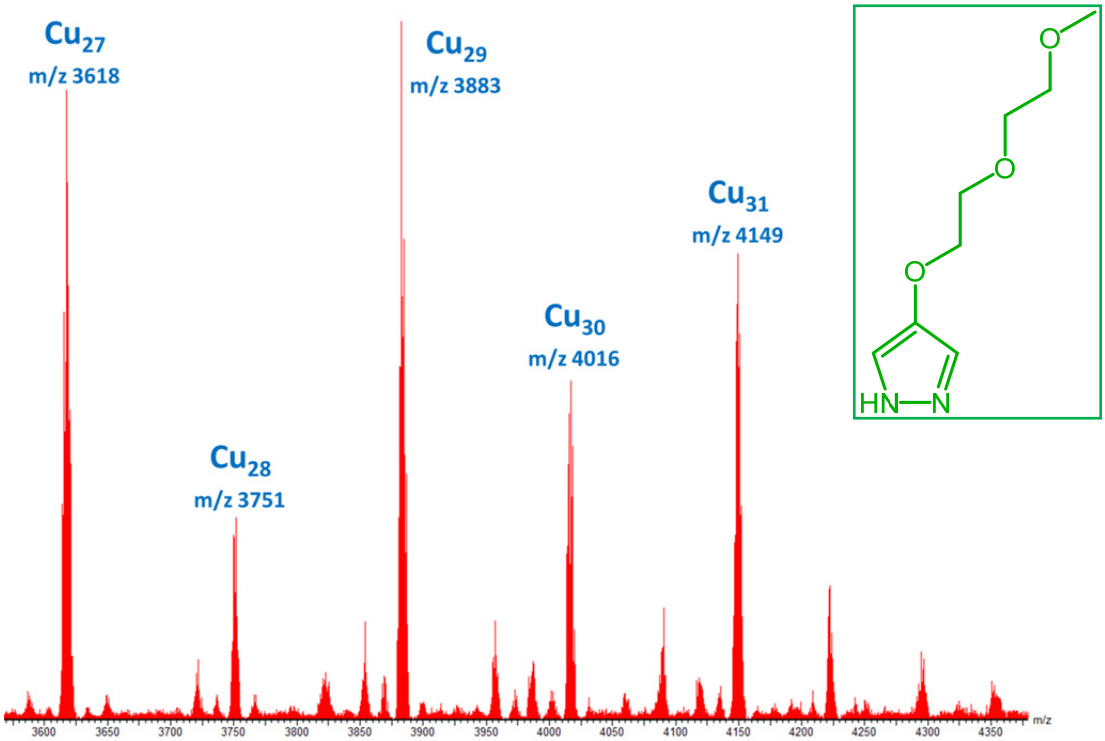

Figure S12. ESI-MS(−) spectrum of $[CO_3 \subset \{Cu(OH)(4\text{-}(CH_3(OCH_2CH_2)_2O)pz)\}_n]^{2-}$ (n = 27−31).

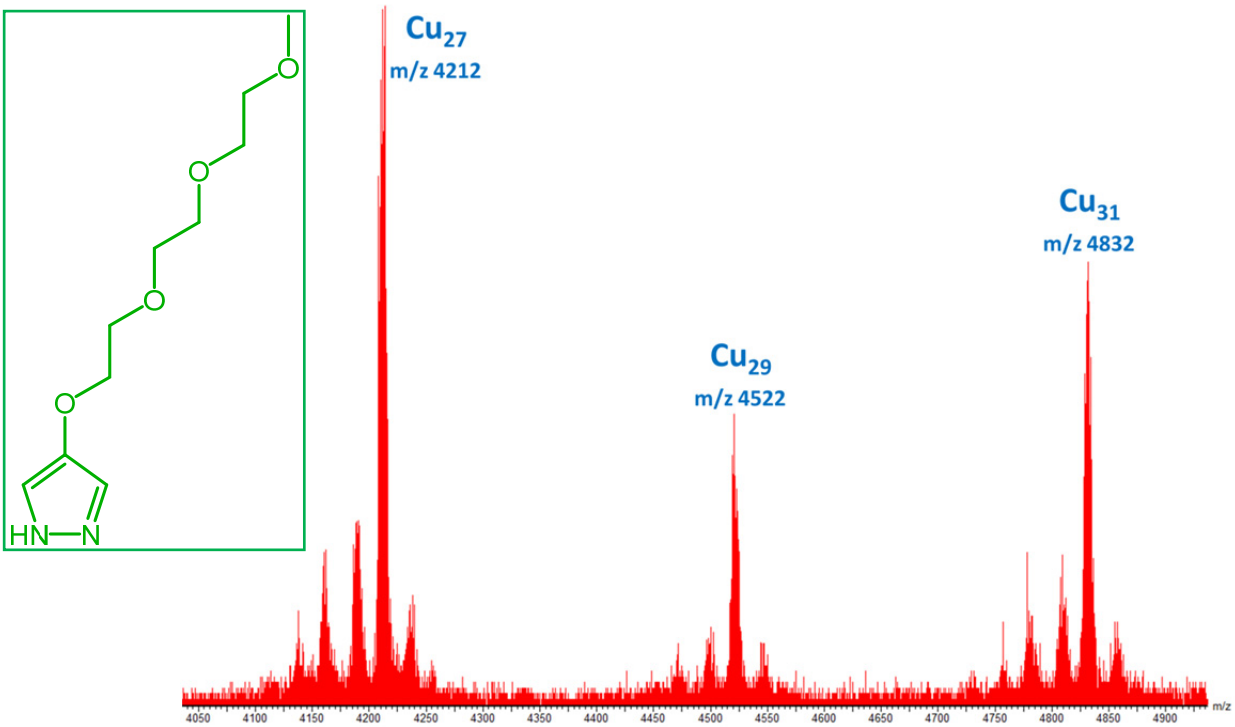

Figure S13. ESI-MS(−) spectrum of $[CO_3 \subset \{Cu(OH)(4\text{-}(CH_3(OCH_2CH_2)_3O)pz)\}_n]^{2-}$ (n = 27, 29, 31).

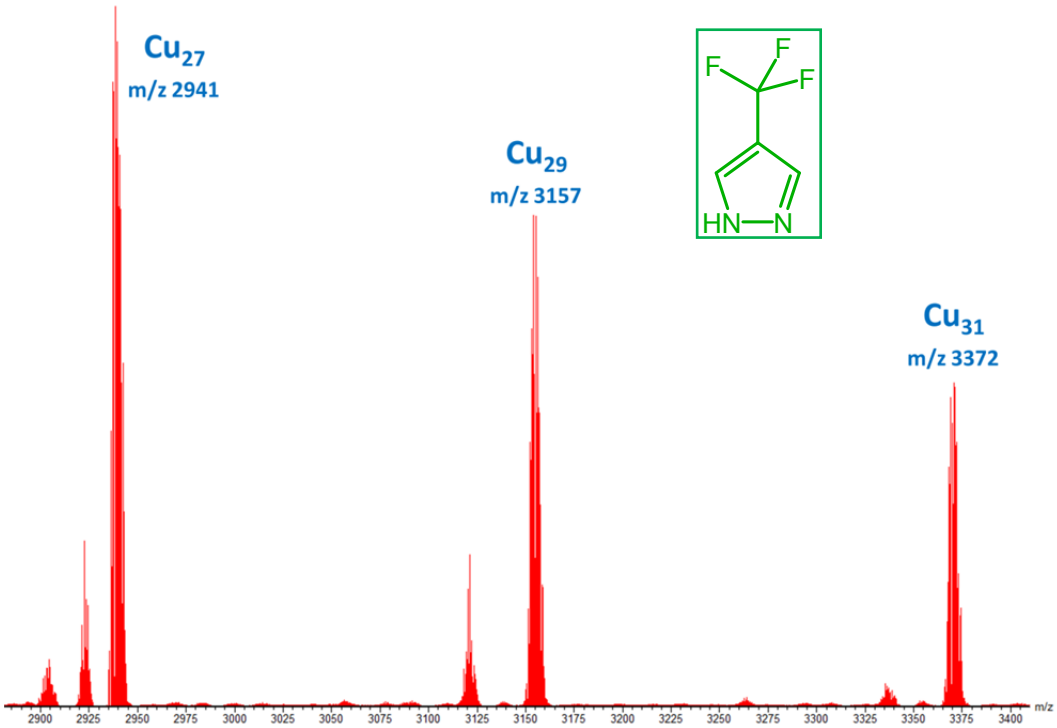

Figure S14. ESI-MS(−) spectrum of $[CO_3 \subset \{Cu(OH)(4\text{-}CF_3pz)\}_n]^{2-}$ (n = 27, 29, 31).

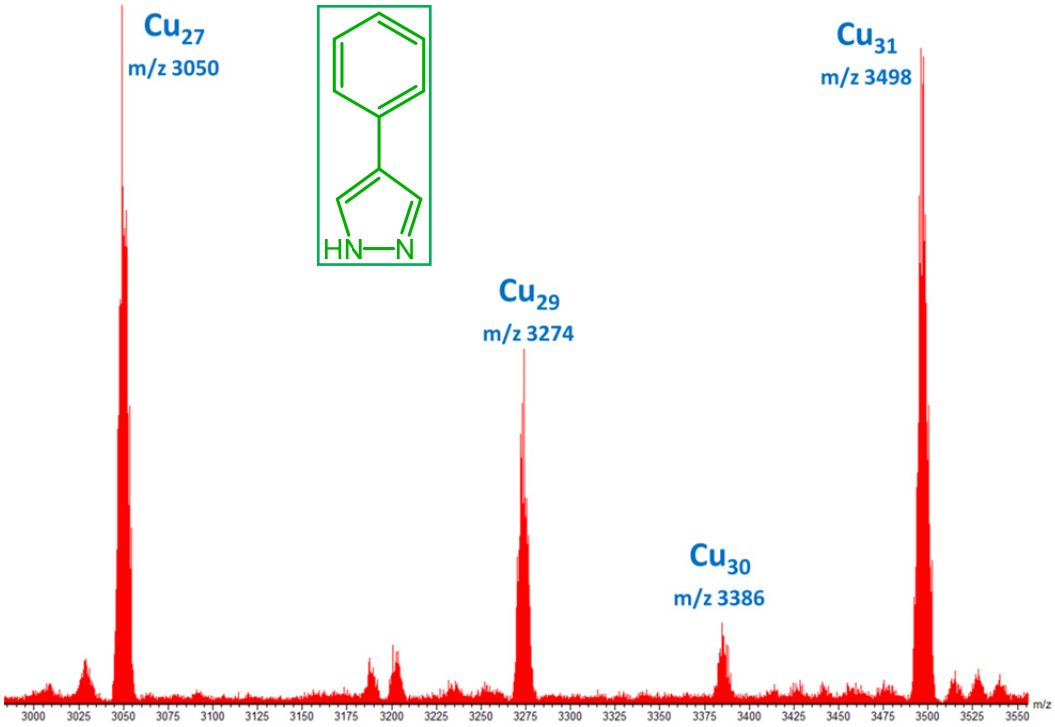

Figure S15. ESI-MS(−) spectrum of $[CO_3 \subset \{Cu(OH)(4\text{-Phpz})\}_n]^{2-}$ (n = 27, 29, 30, 31).

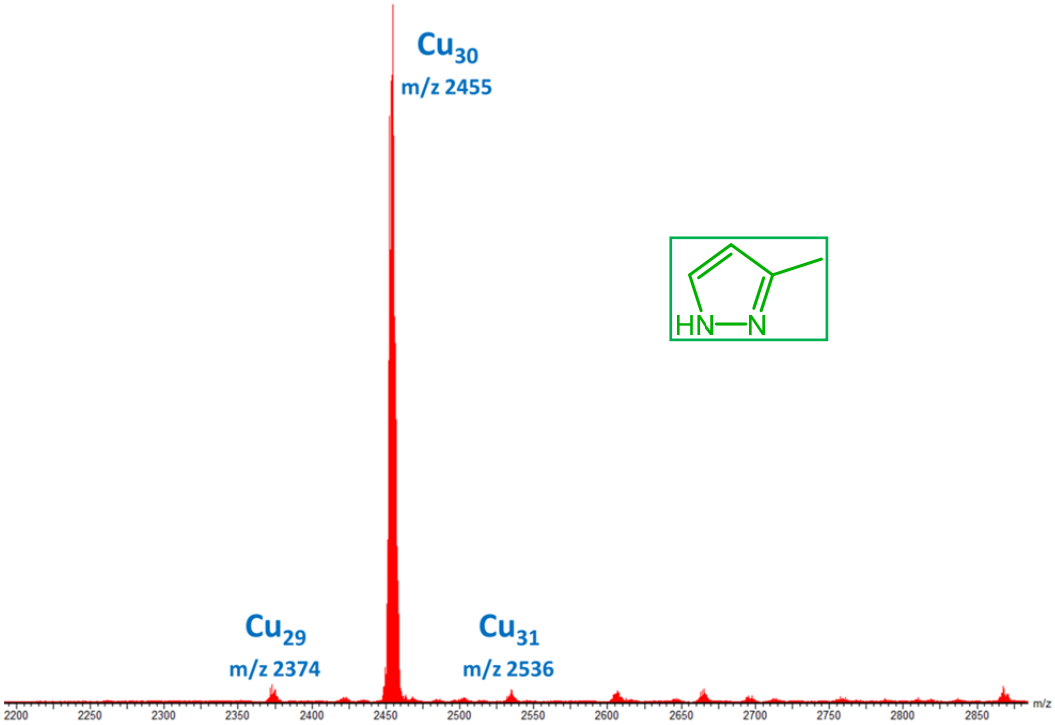

Figure S16. ESI-MS(−) spectrum of $[CO_3 \subset \{Cu(OH)(3\text{-Mepz})\}_n]^{2-}$ (n = 29, 30, 31).

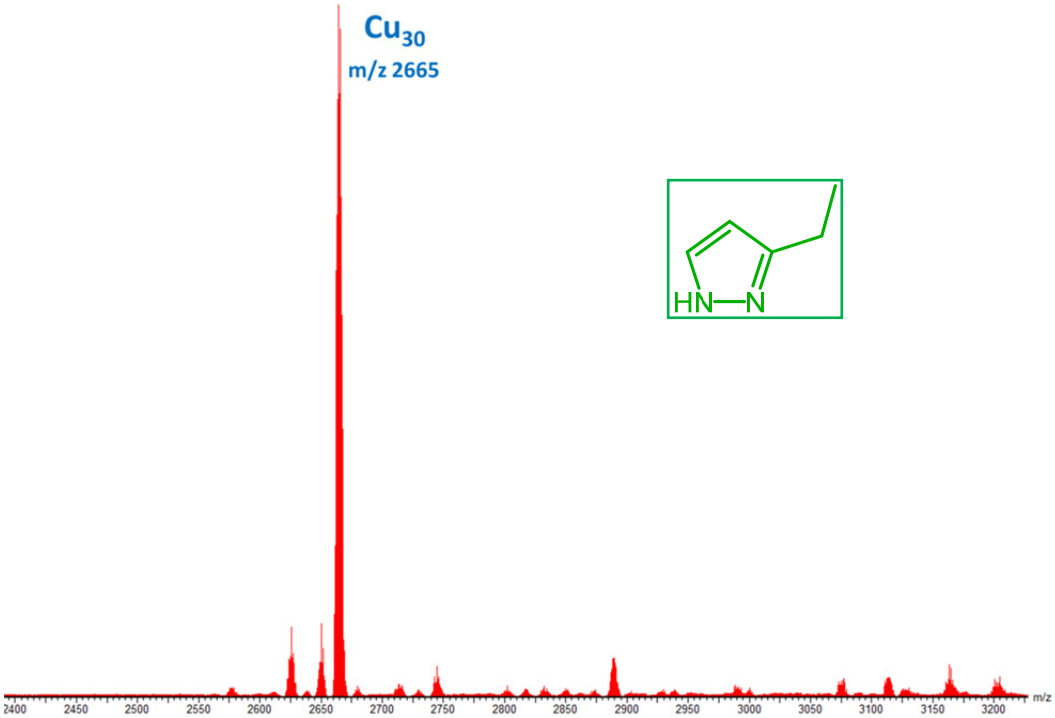

Figure S17. ESI-MS(−) spectrum of $[CO_3 \subset \{Cu(OH)(3\text{-Etpz})\}_n]^{2-}$ (n = 30).

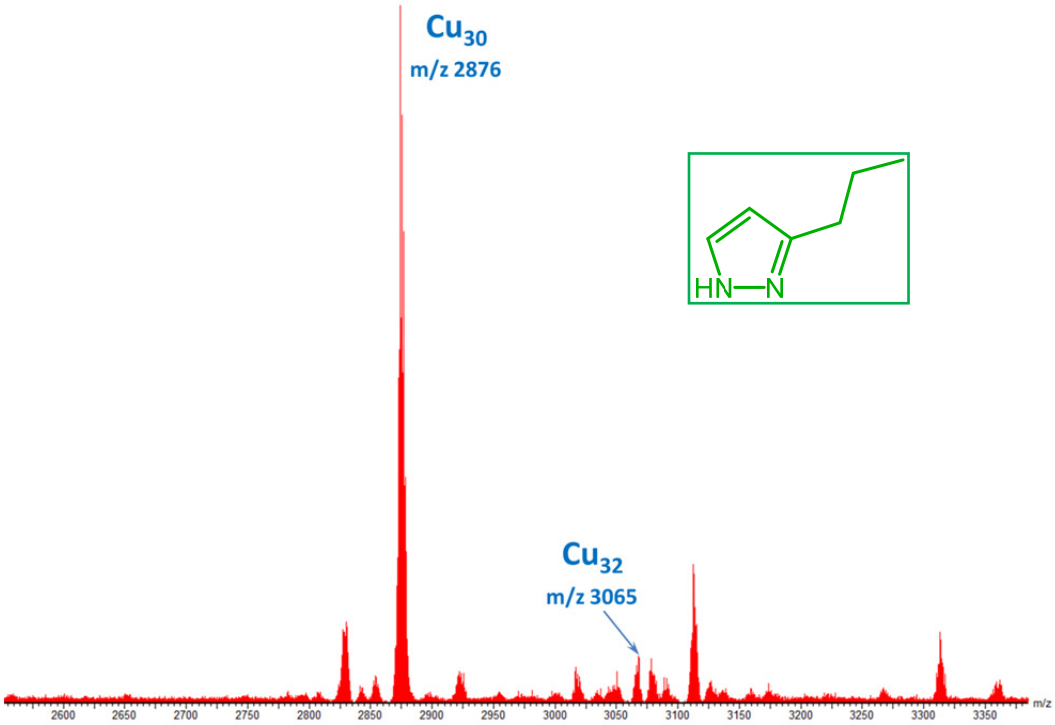

Figure S18. ESI-MS(−) spectrum of $[CO_3 \subset \{Cu(OH)(3\text{-}^{n}\text{Prpz})\}_n]^{2-}$ (n = 30, 32).

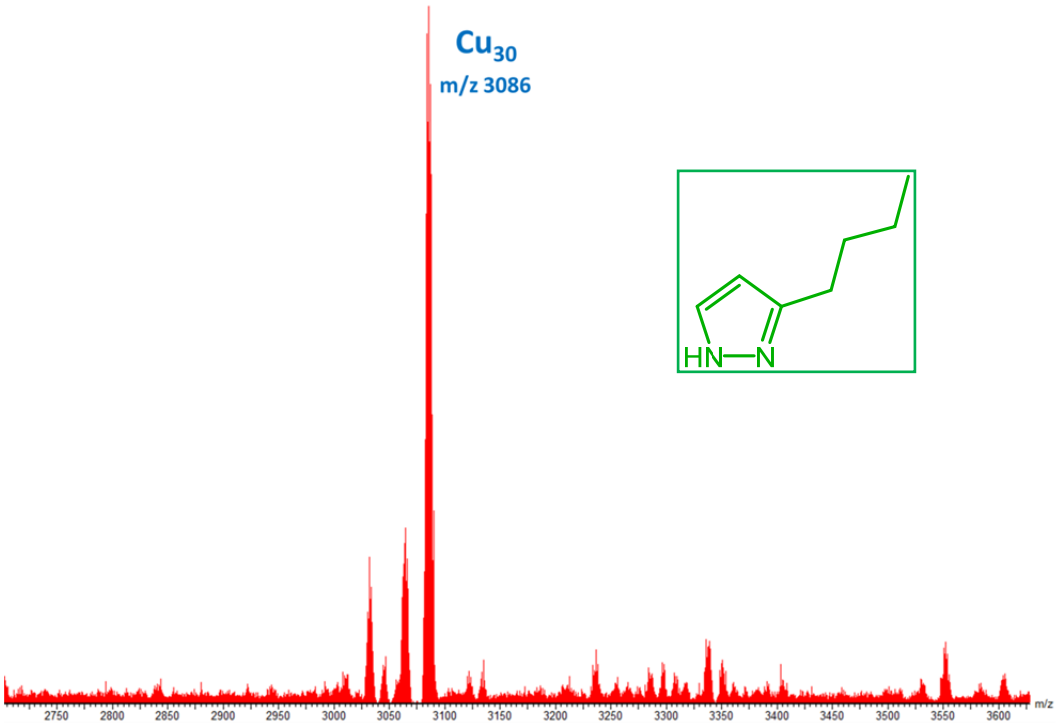

Figure S19. ESI-MS(−) spectrum of $[CO_3 \subset \{Cu(OH)(3\text{-}^{n}Bupz)\}_n]^{2-}$ (n = 30).

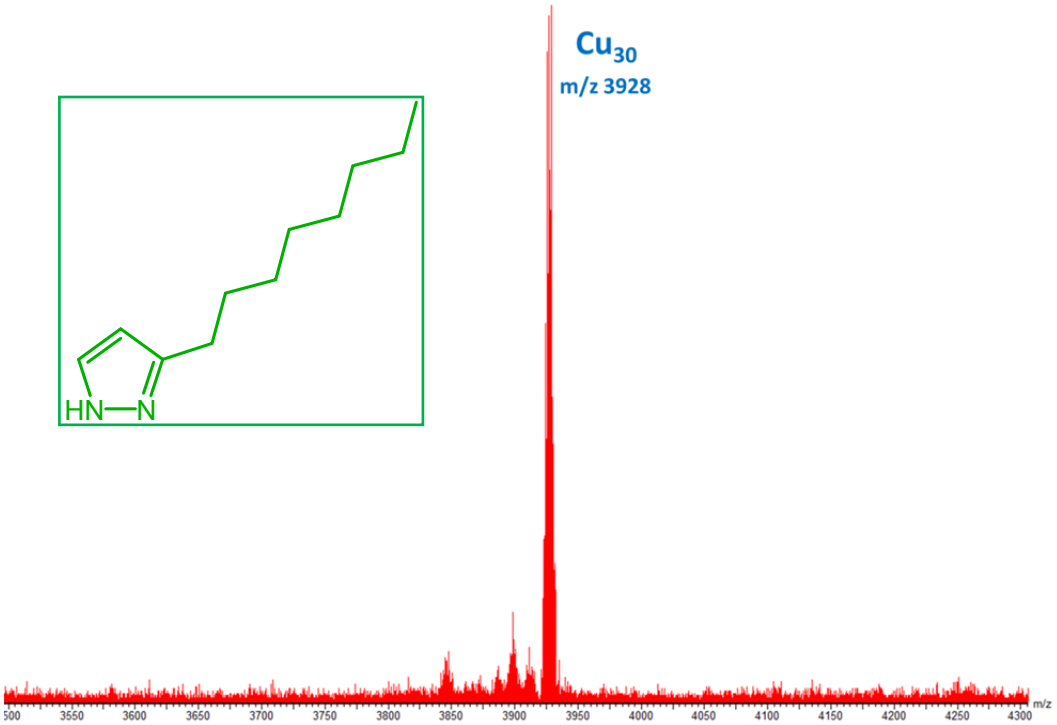

Figure S20. ESI-MS(−) spectrum of $[CO_3 \subset \{Cu(OH)(3\text{-}^{n}Octpz)\}_n]^{2-}$ (n = 30).

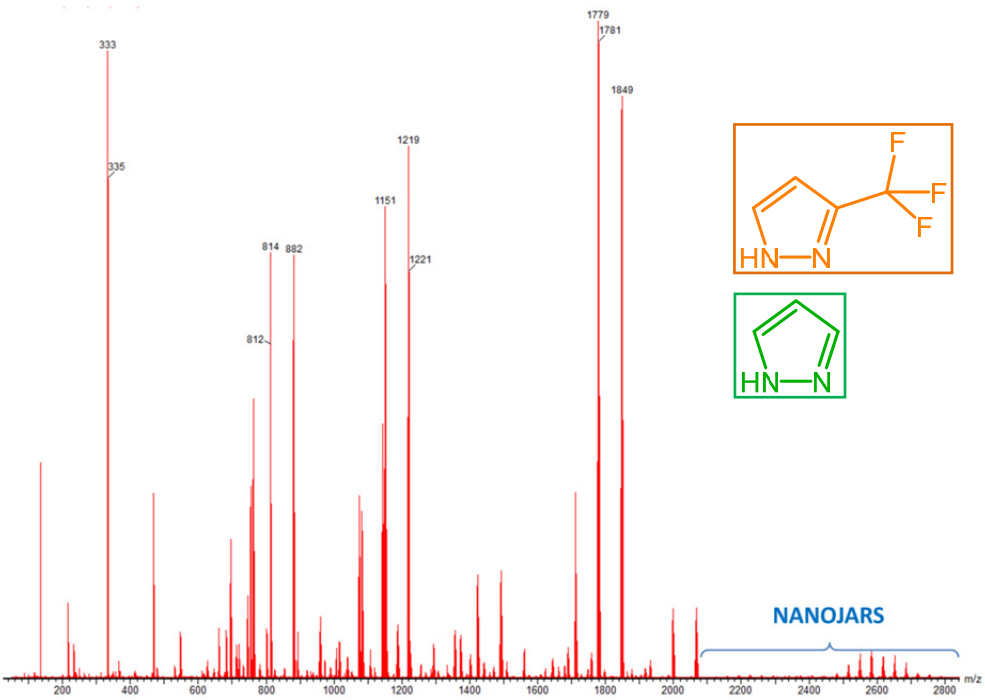

Figure S21. ESI-MS(−) spectrum of the product mixture obtained from $Cu(NO_3)_2$, 3-CF_3pzH/HpzH (1:1), NaOH, Bu_4NOH and Na_2CO_3 (see $[CO_3\subset\{Cu_n(OH)_n(3\text{-}CF_3pz)_y(pz)_{n-y}\}]^{2-}$ species below).

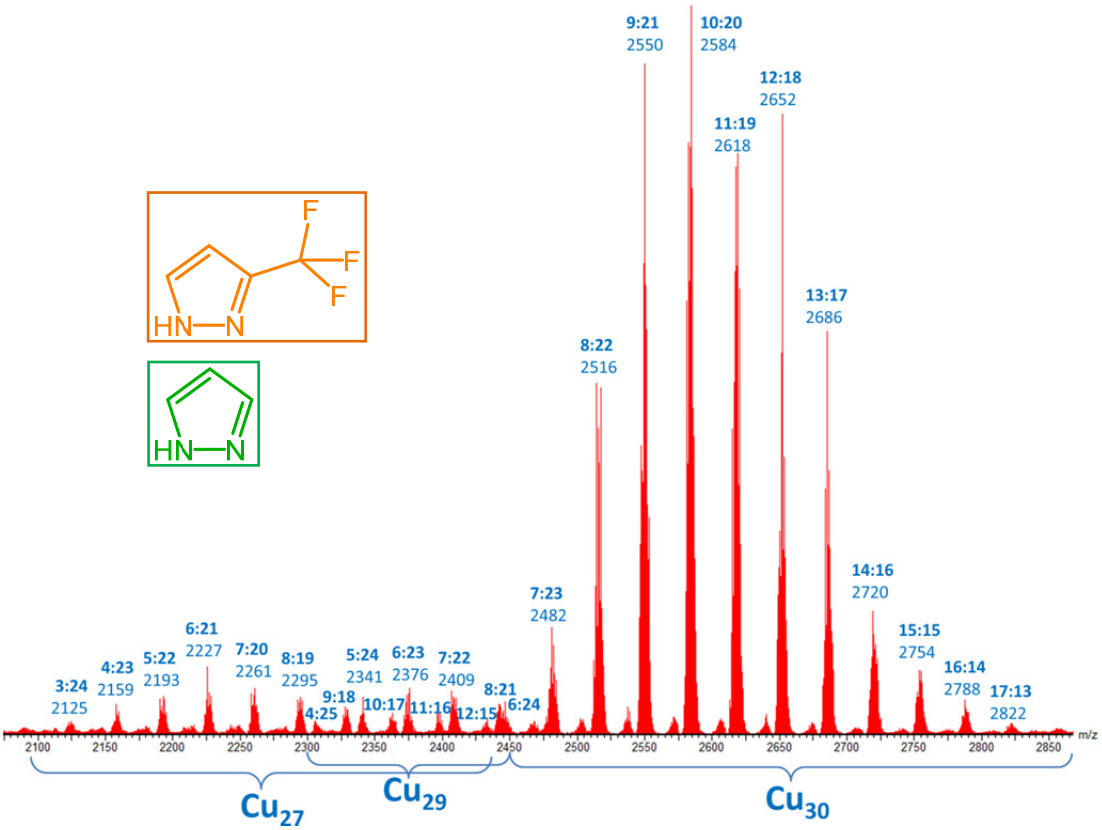

Figure S22. $[CO_3\subset\{Cu_n(OH)_n(3\text{-}CF_3pz)_y(pz)_{n-y}\}]^{2-}$ species observed (y:n−y & *m/z* shown).

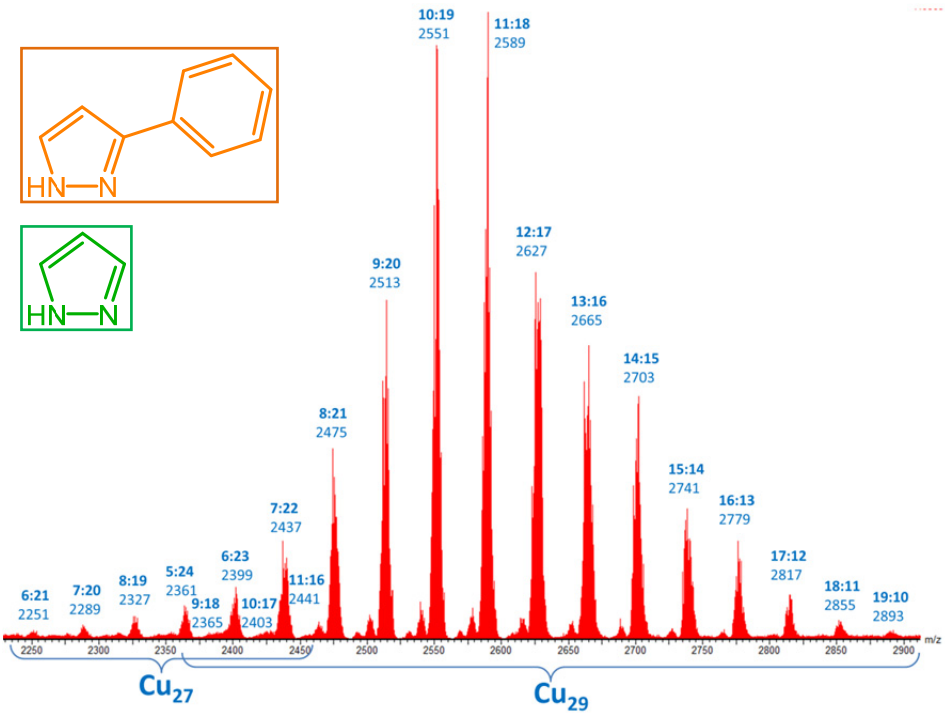

Figure S23. ESI-MS(−) spectrum of $[CO_3{\subset}\{Cu_n(OH)_n(3\text{-Phpz})_y(pz)_{n-y}\}]^{2-}$ (y:n−y & *m/z* shown).

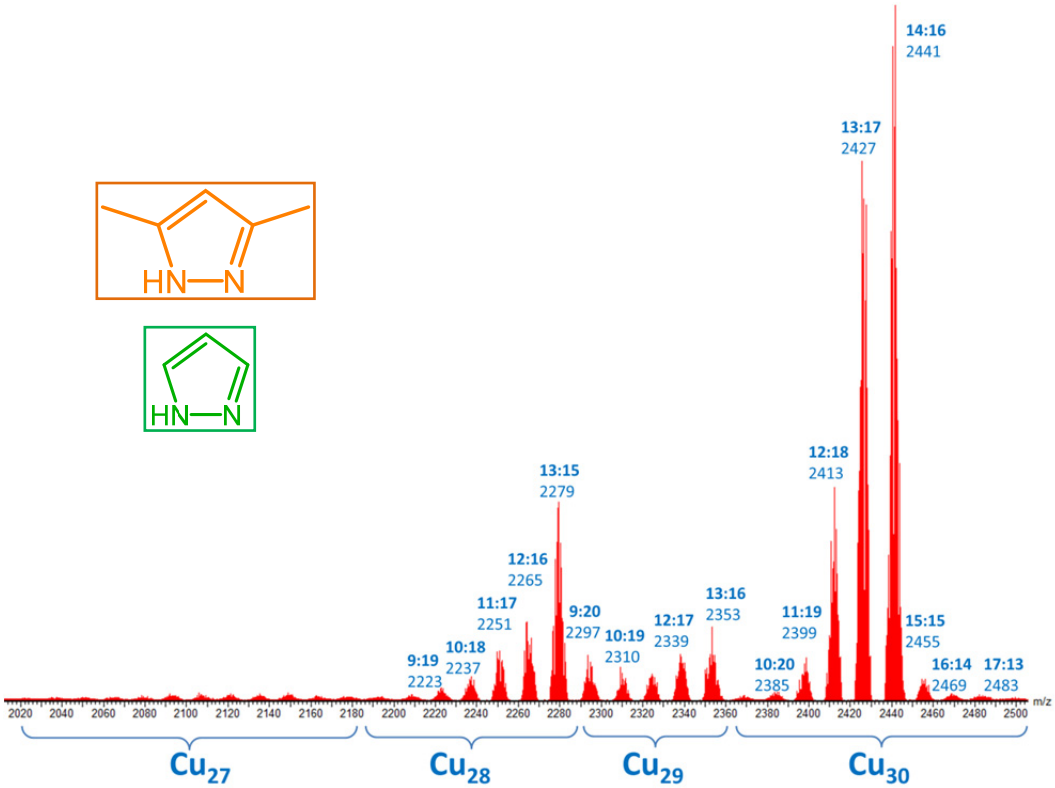

Figure S24. ESI-MS(−) spectrum of $[CO_3{\subset}\{Cu_n(OH)_n(3,5\text{-Me}_2pz)_y(pz)_{n-y}\}]^{2-}$ (y:n−y & *m/z* shown) obtained from $Cu(NO_3)_2$, 3,5-Me_2pzH/HpzH (1:1), NaOH, Bu_4NOH and Na_2CO_3.

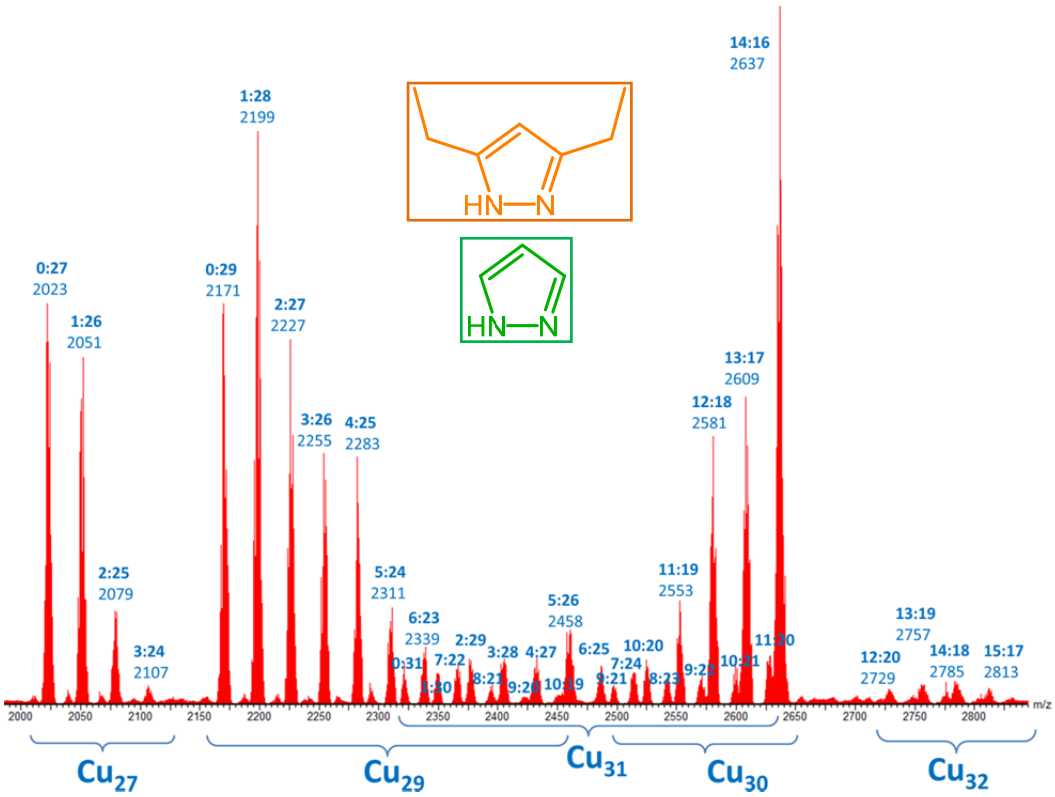

Figure S25. ESI-MS(−) spectrum of $[CO_3{\subset}\{Cu_n(OH)_n(3,5\text{-}Et_2pz)_y(pz)_{n-y}\}]^{2-}$ (y:n−y & *m/z* shown).

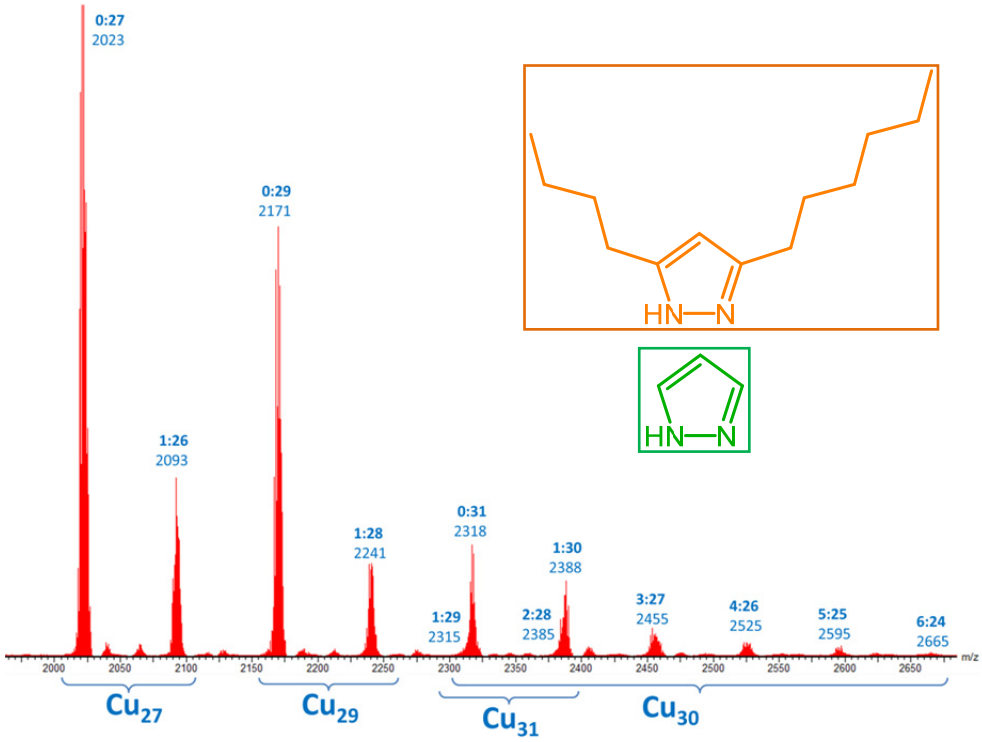

Figure S26. ESI-MS(−) spectrum of $[CO_3{\subset}\{Cu_n(OH)_n(3\text{-}^{n}Bu\text{-}5\text{-}^{n}Hexpz)_y(pz)_{n-y}\}]^{2-}$ (y:n−y & *m/z* shown).

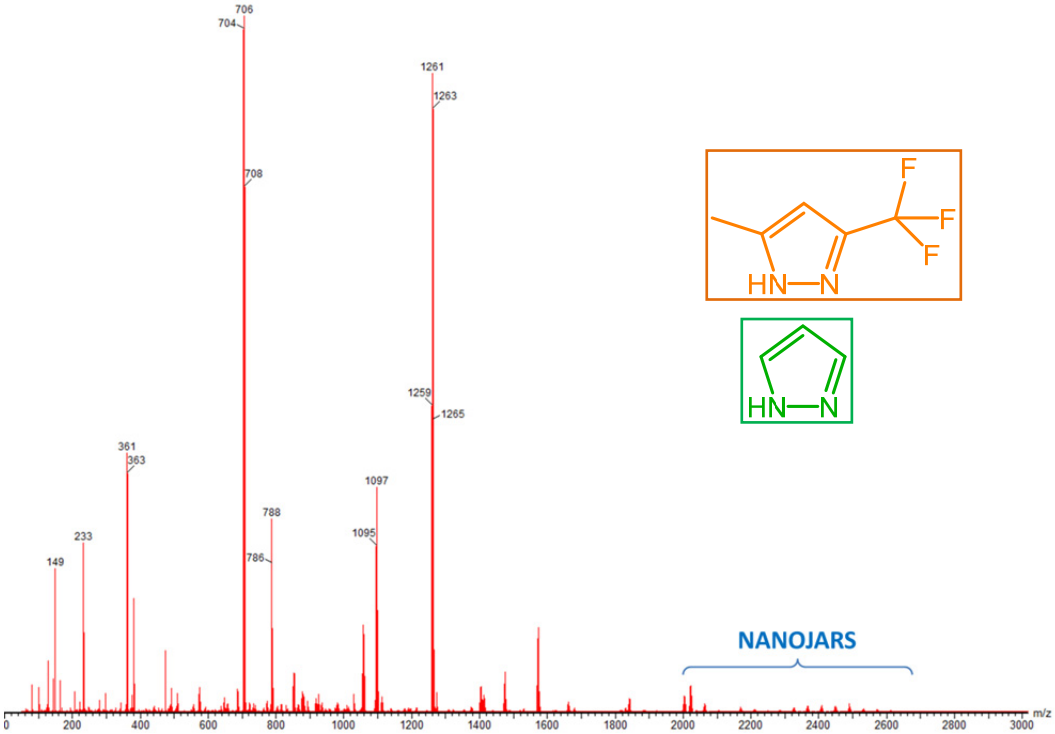

Figure S27. ESI-MS(−) spectrum of the product mixture obtained from $Cu(NO_3)_2$, 3-Me-5-CF_3pzH/HpzH (1:1), NaOH, Bu_4NOH and Na_2CO_3 (see $[CO_3{\subset}\{Cu_n(OH)_n(3\text{-Me-5-}CF_3pz)_y(pz)_{n-y}\}]^{2-}$ species below).

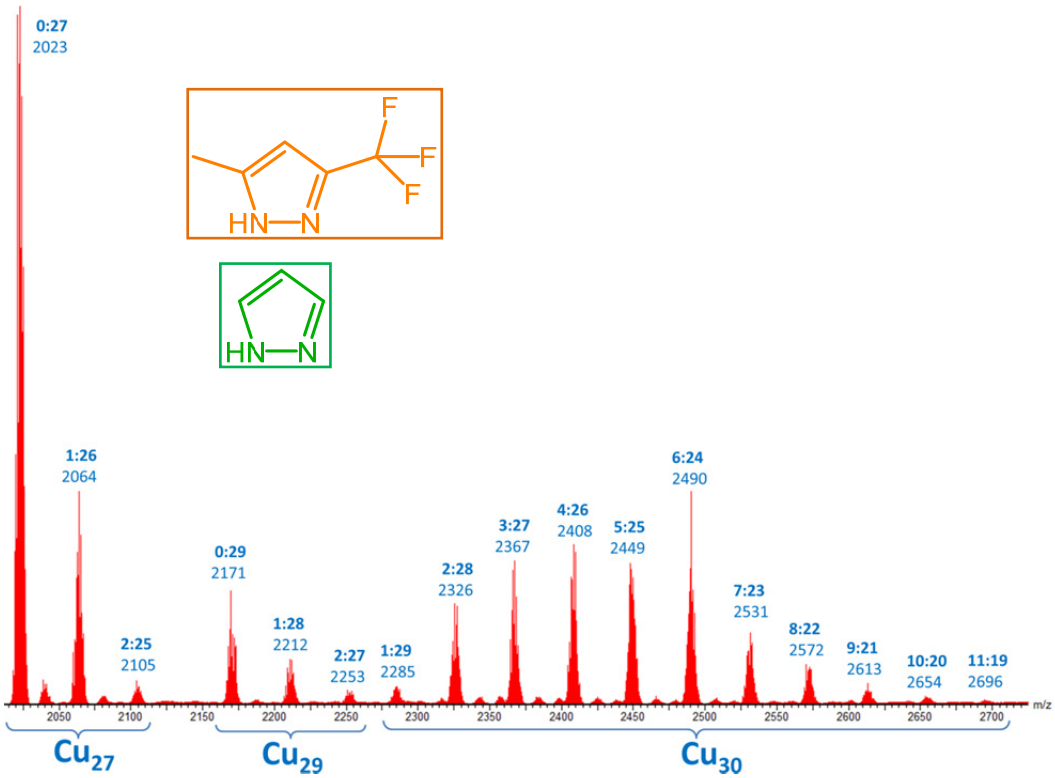

Figure S28. $[CO_3{\subset}\{Cu_n(OH)_n(3\text{-Me-5-}CF_3pz)_y(pz)_{n-y}\}]^{2-}$ species observed (y:n−y & *m/z* shown).

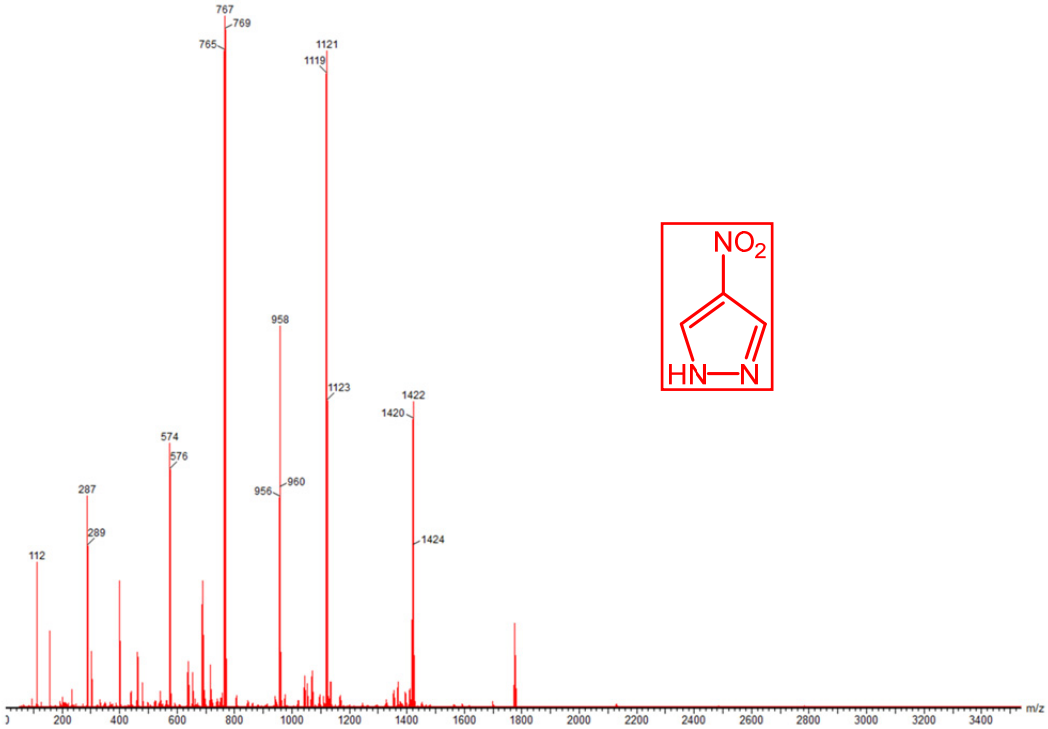

Figure S29. ESI-MS(−) spectrum of the product mixture obtained from $Cu(NO_3)_2$, 4-NO_2pzH, NaOH, Bu_4NOH and Na_2CO_3.

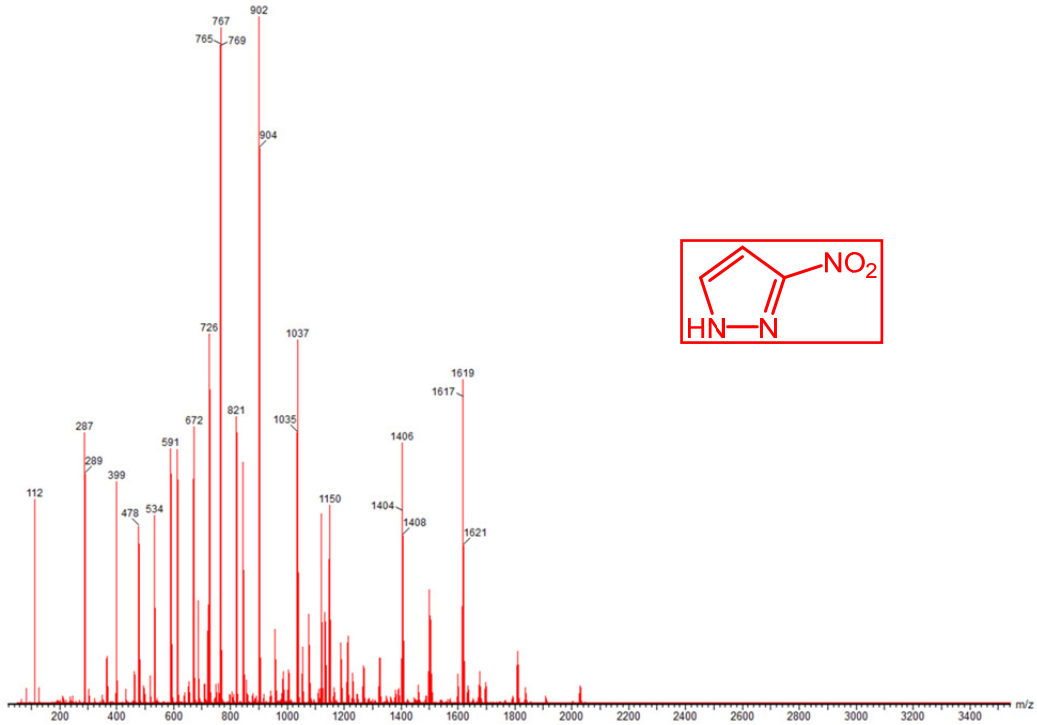

Figure S30. ESI-MS(−) spectrum of the product mixture obtained from $Cu(NO_3)_2$, 3-NO_2pzH, NaOH, Bu_4NOH and Na_2CO_3.

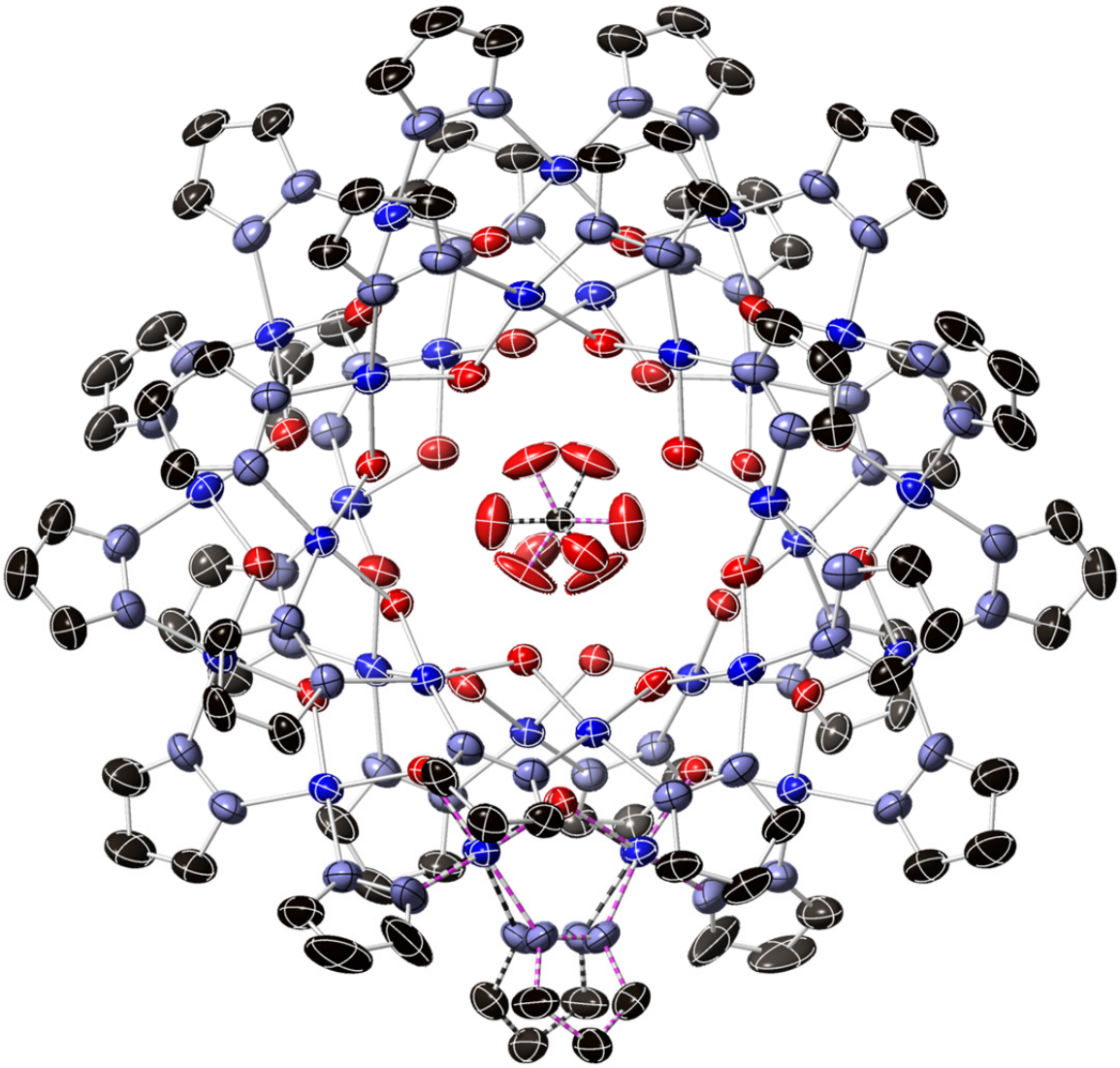

Figure S31. Thermal ellipsoid plot (50% probability) of Et_4N-**1**·$2H_2O$. H-atoms, counterions and solvent molecules are omitted for clarity. Color code: Cu−dark blue; O−red; N−light blue; C−black.

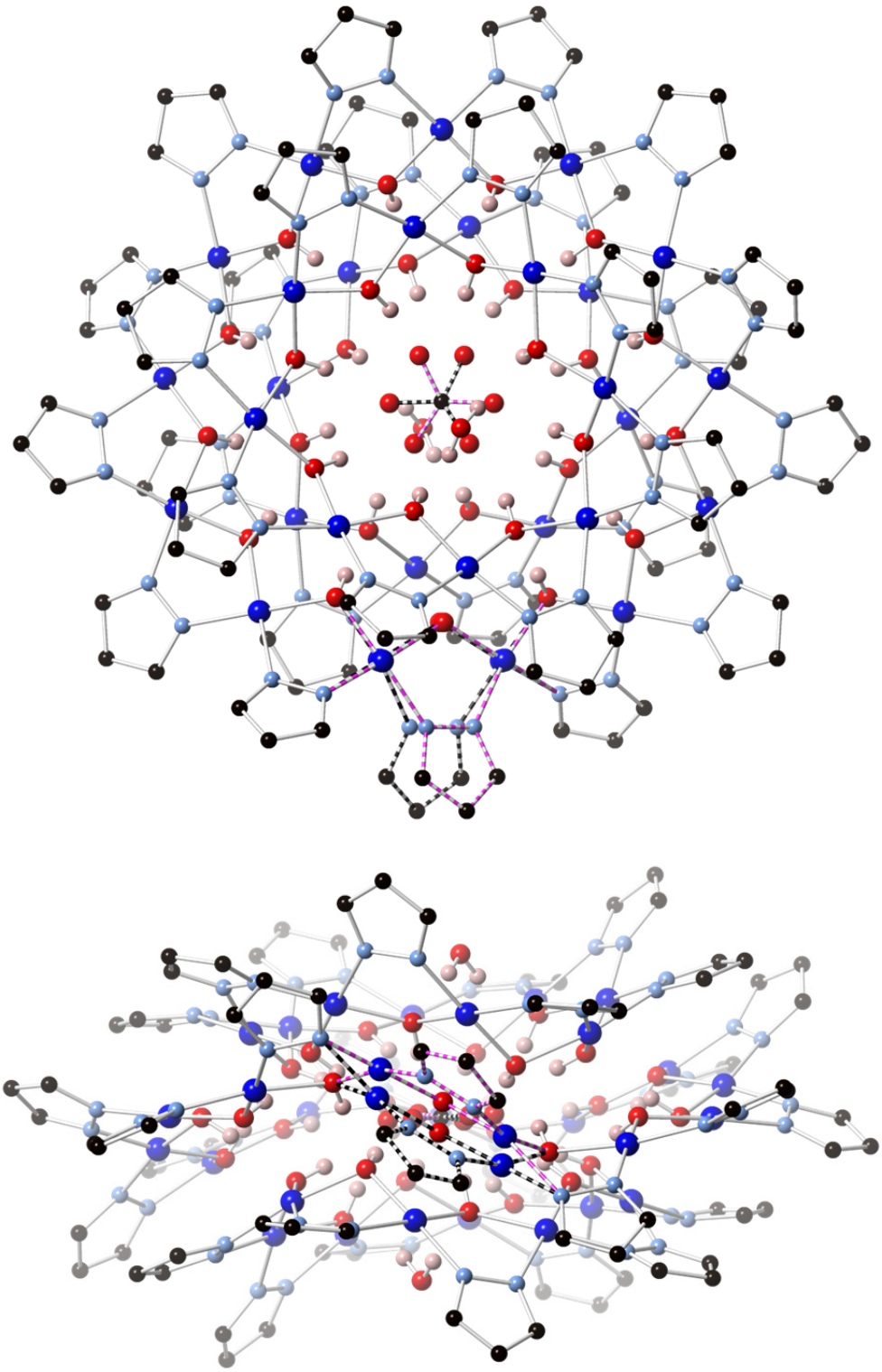

Figure S32. Ball-and-stick representation (top- and side-views) of Et_4N-**1**·$2H_2O$, showing the position of the disordered pyrazole and carbonate units. Color code: Cu−dark blue; O−red; N−light blue; C−black; H−pink. C−H hydrogen atoms, solvent and counterion molecules are omitted for clarity.

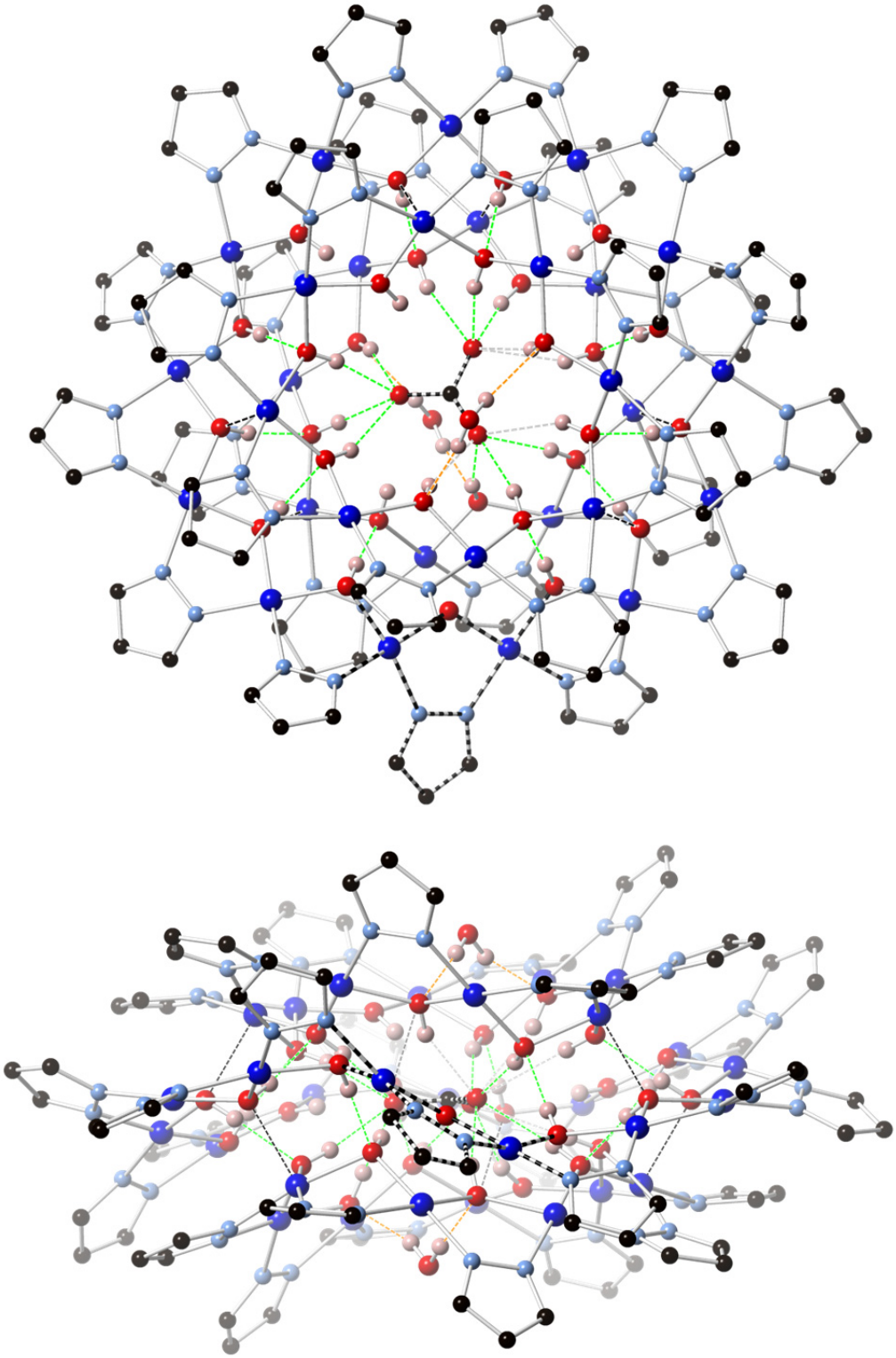

Figure S33. Top- and side-views of Et_4N-**1**·$2H_2O$, showing the hydrogen-bonding pattern (green dashed lines; orange for the H_2O molecules) and axial Cu-O interactions (black dashed lines). Color code: Cu−dark blue; O−red; N−light blue; C−black; H−pink. Only one position of the disordered pyrazole and carbonate units is shown. C−H hydrogen atoms, solvent and counterion molecules are omitted for clarity.

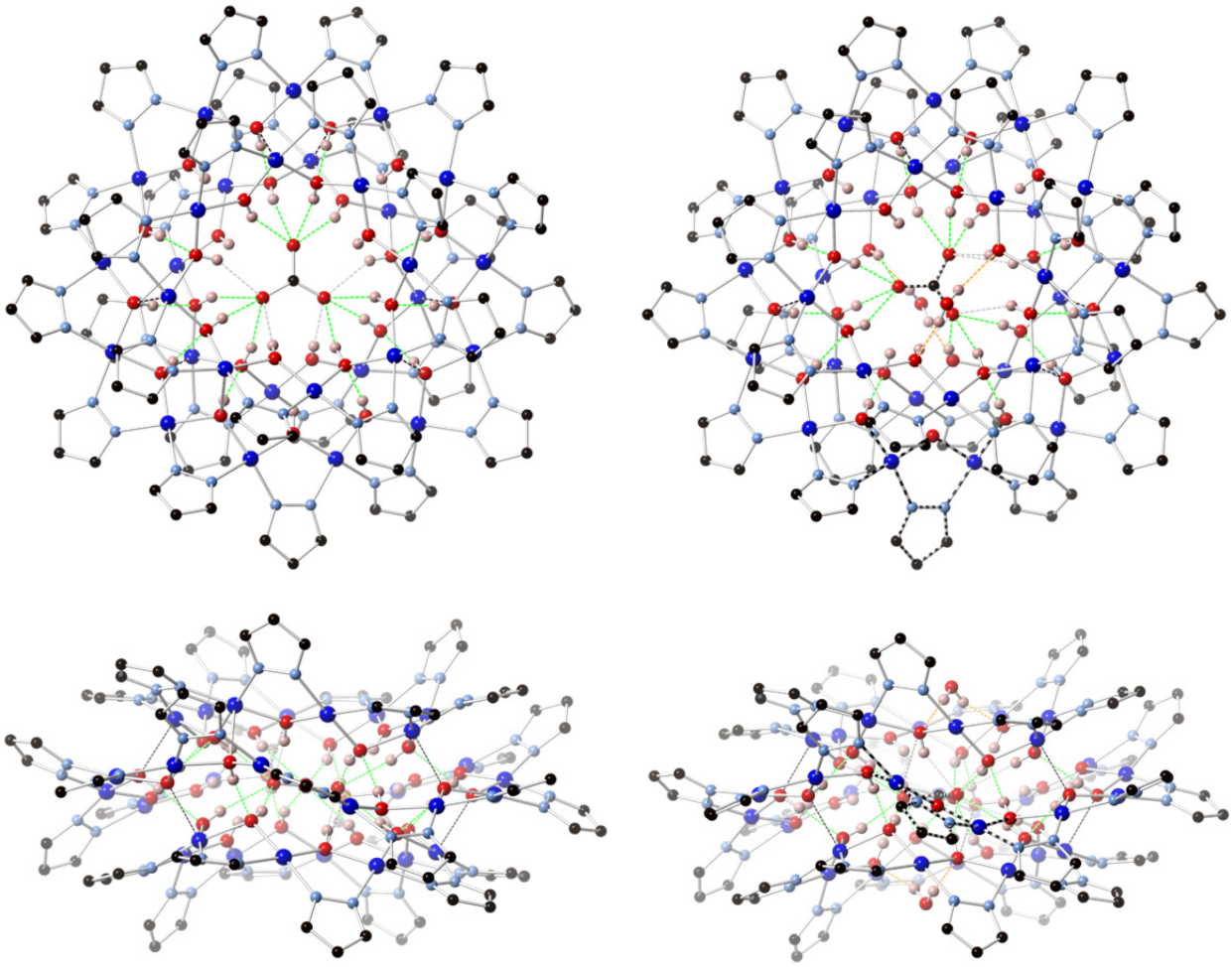

Figure S34. Comparison (top- and side-views) of the near-identical structures of Bu_4N-**1** (left) and Et_4N-**1**·$2H_2O$ (right; only one position of the disordered pyrazole and carbonate units is shown).

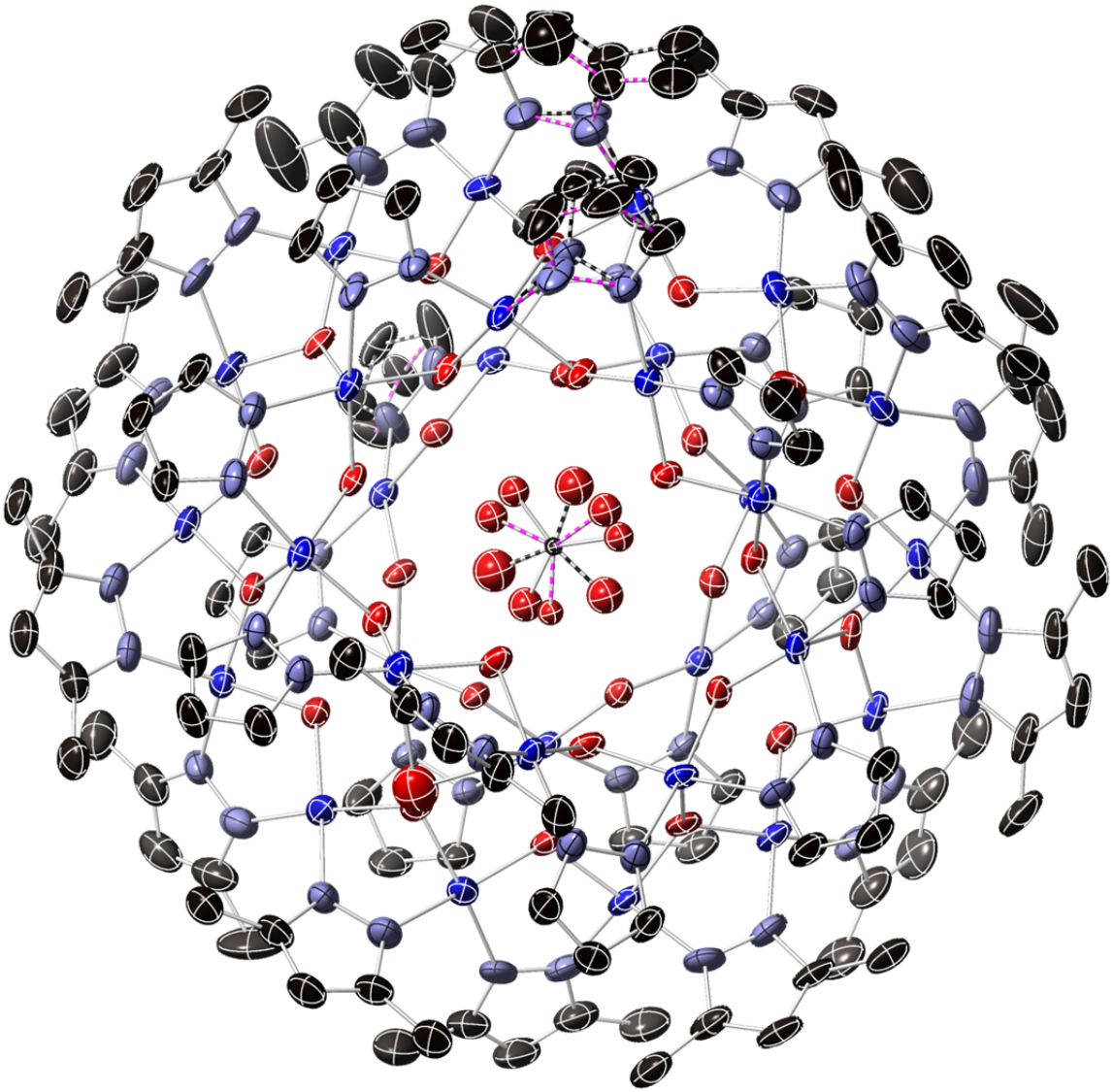

Figure S35. Thermal ellipsoid plot (50% probability) of **2**. H-atoms, counterions and solvent molecules are omitted for clarity. Color code: Cu−dark blue; O−red; N−light blue; C−black.

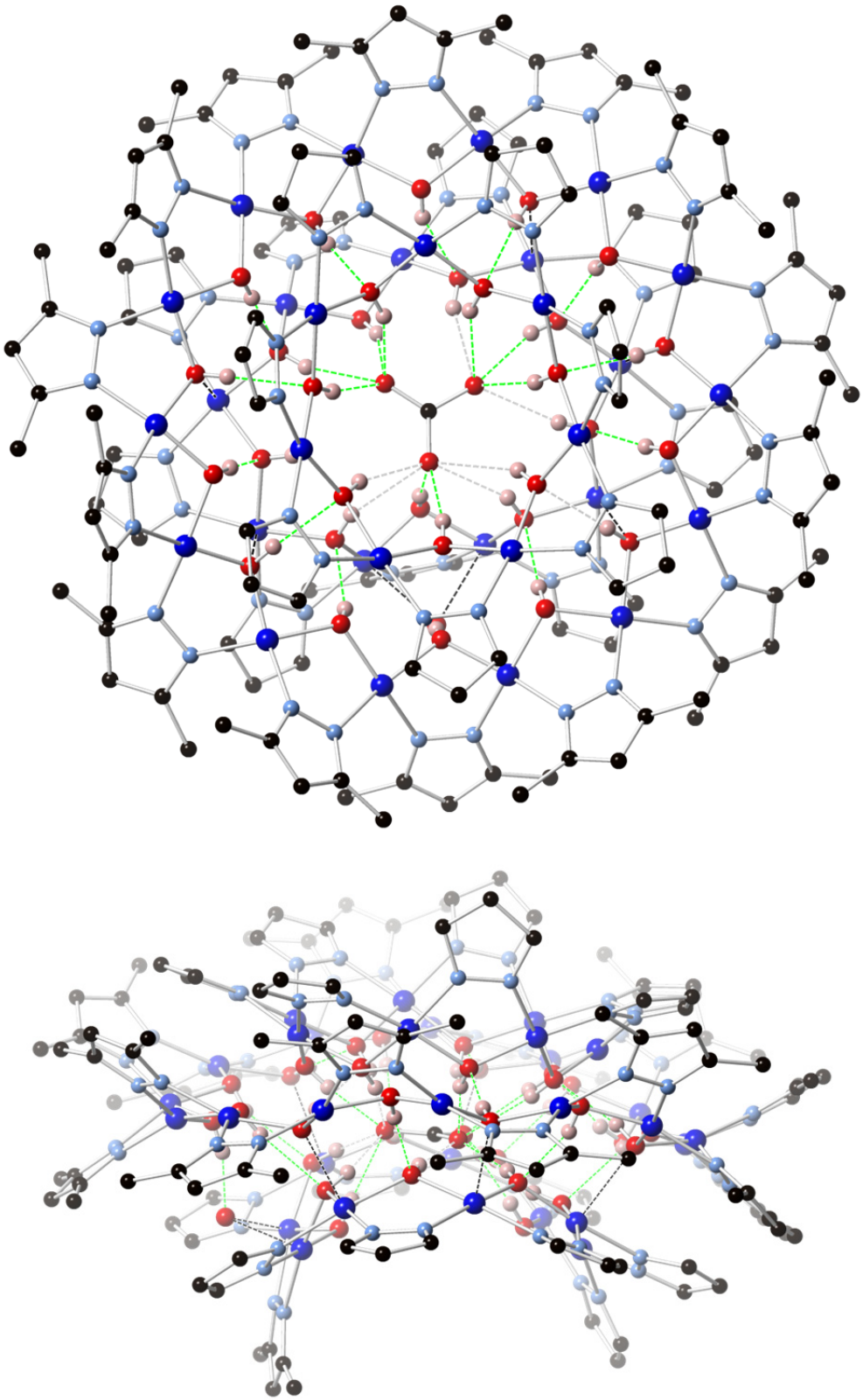

Figure S36. Top- and side-views of **2** (for clarity, only the major component of the disordered units is shown). H-bonds are shown as green dashed lines, and weak Cu−O bonds as black dashed lines.

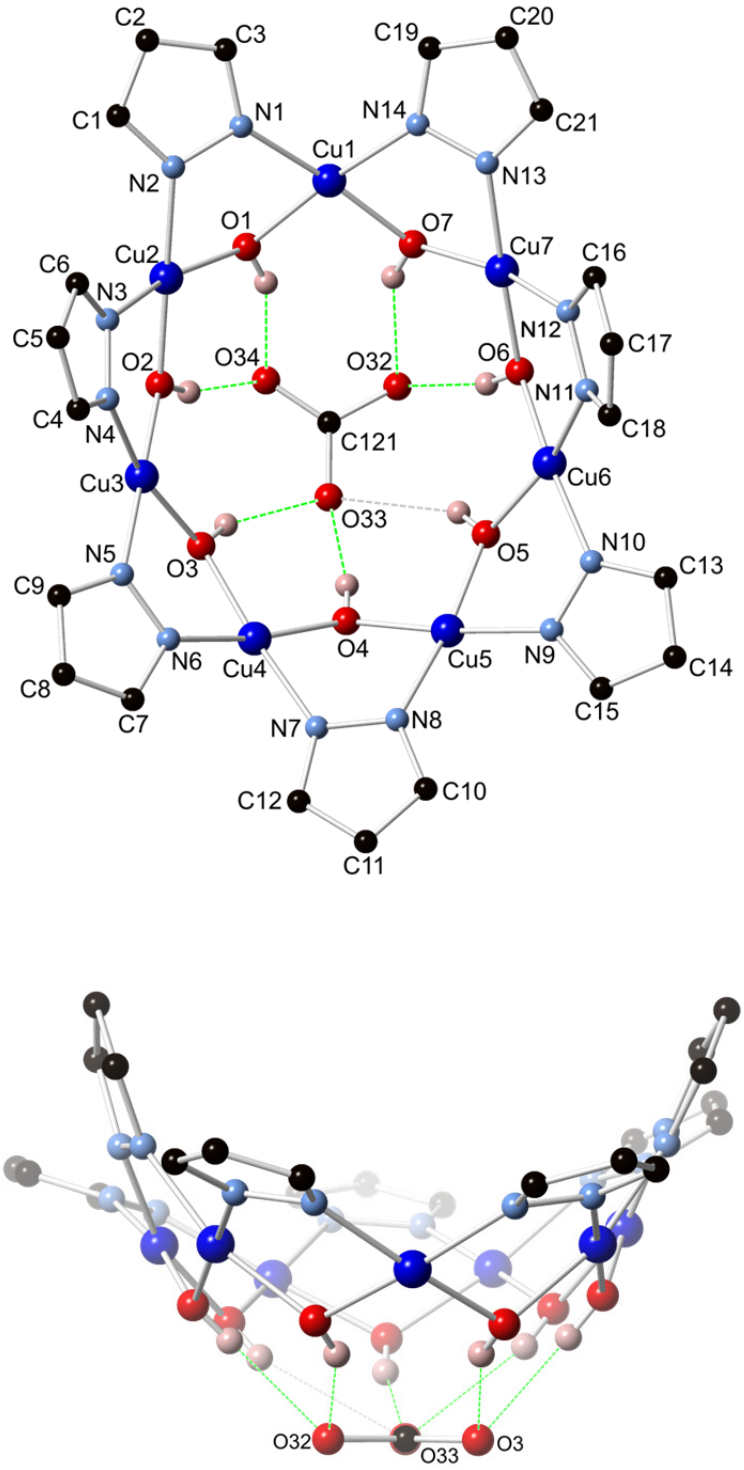

Figure S37. Top- and side-views of the Cu_7-ring in **2**, showing hydrogen-bonding (green dashed lines for O···O distances <3.00(5) Å, grey dashed lines for O···O distances 3.00(5)−3.20(5) Å) to the carbonate ion (only the major component of the disordered units is shown).

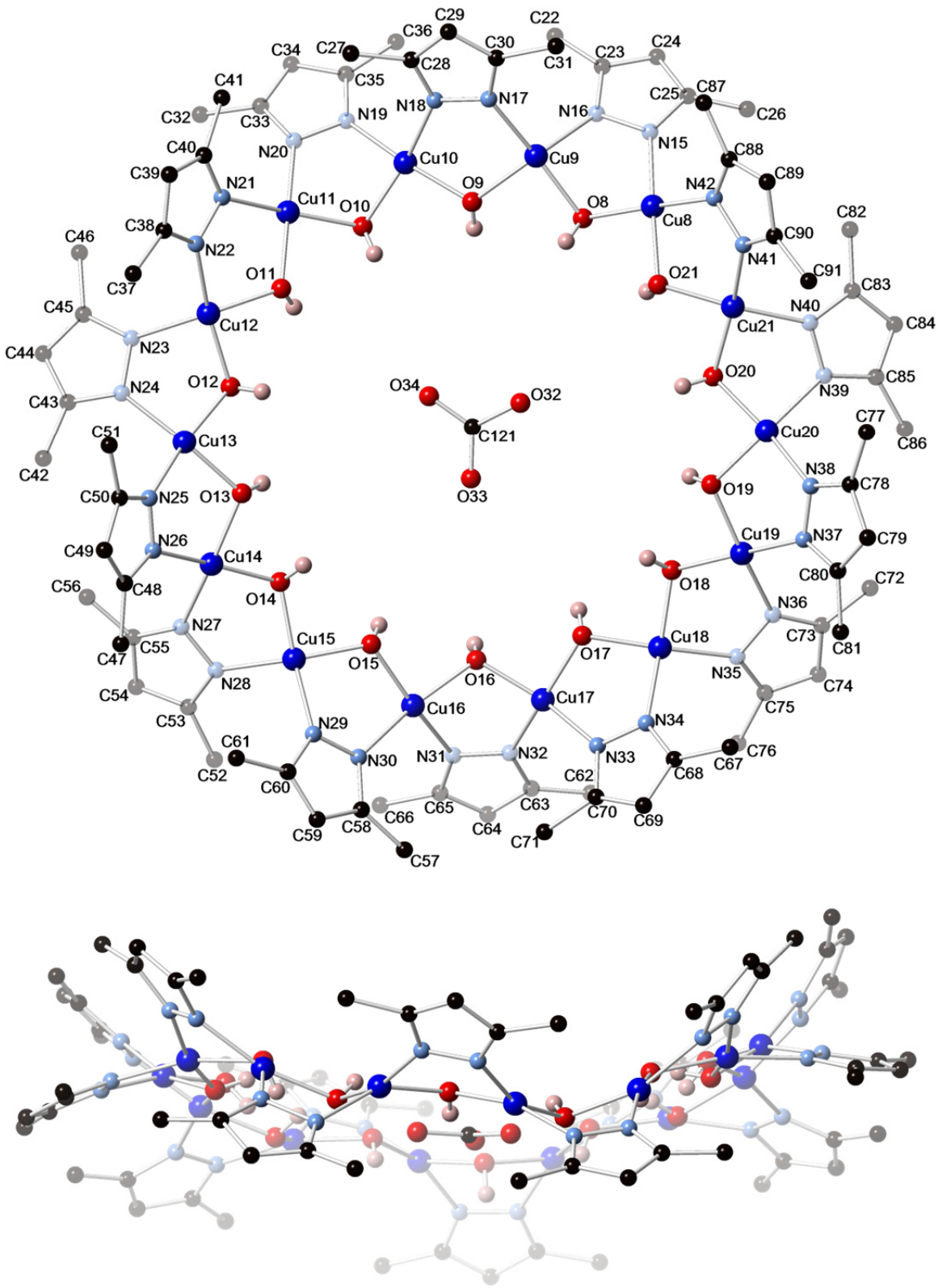

Figure S38. Top- and side-views of the Cu_{14}-ring in **2**, with the carbonate ion at the center (only the major component of the disordered units is shown).

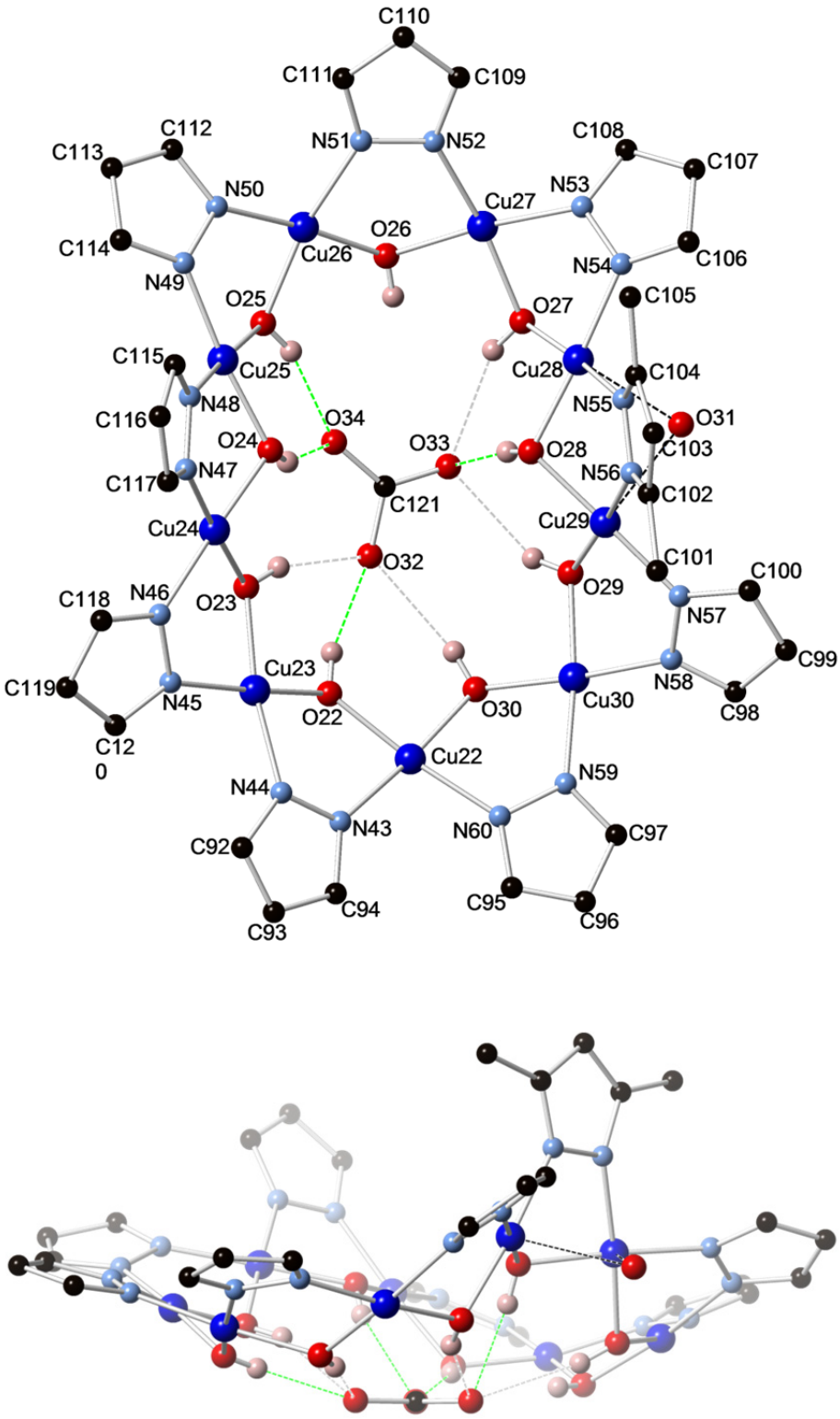

Figure S39. Top- and side-views of the Cu_9-ring in **2**, showing hydrogen-bonding (green dashed lines for O···O distances <3.00(5) Å, grey dashed lines for O···O distances 3.00(5)−3.20(5) Å) to the carbonate ion (only the major component of the disordered units is shown). Cu−O bonds to the H_2O molecule are shown with black dashed lines.

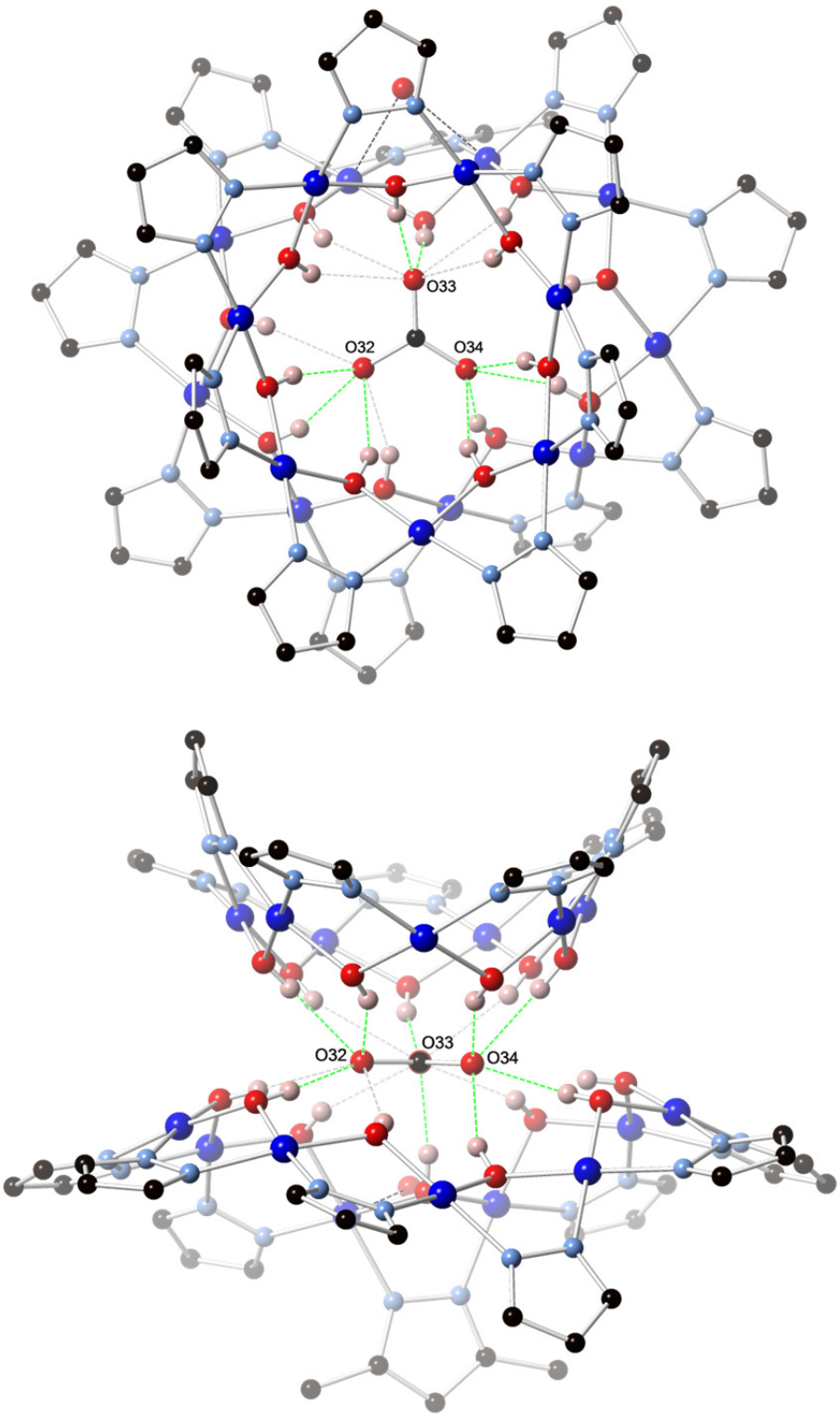

Figure S40. Top- and side-views of the Cu_7- and Cu_9-rings in **2**, showing hydrogen-bonding (green dashed lines for O···O distances <3.00(5) Å, grey dashed lines for O···O distances 3.00(5)−3.20(5) Å) to the carbonate ion (only the major component of the disordered units is shown). Cu−O bonds to the H_2O molecule are shown with black dashed lines.

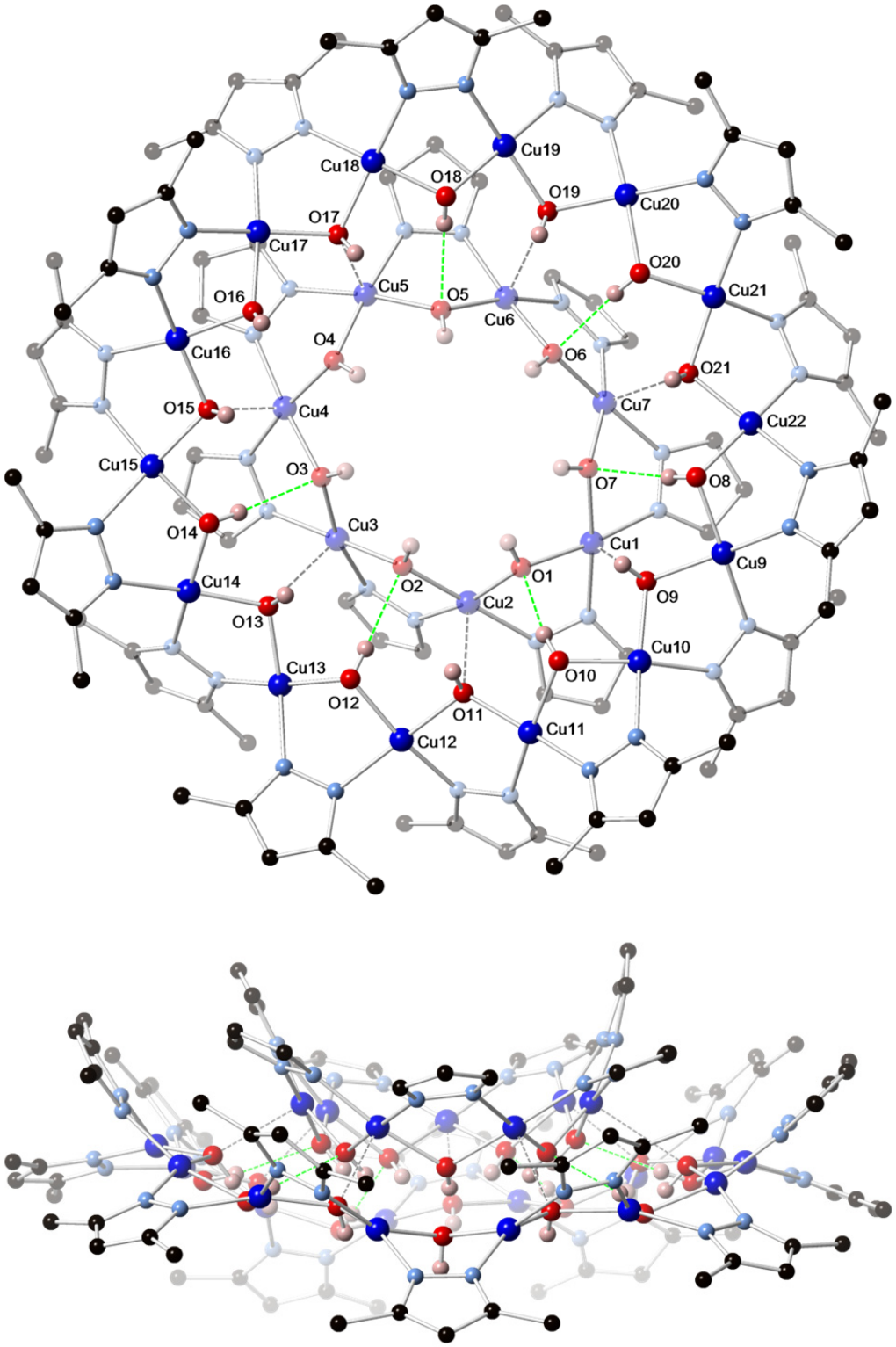

Figure S41. Top- and side-views of the Cu_7- and Cu_{14}-rings in **2**, showing hydrogen-bonding (green dashed lines for O···O distances <3.00(5) Å, grey dashed lines for O···O distances 3.00(5)−3.20(5) Å) and axial Cu-O interactions (black dashed lines for Cu···O distances <2.50 Å) (only the major component of the disordered units is shown).

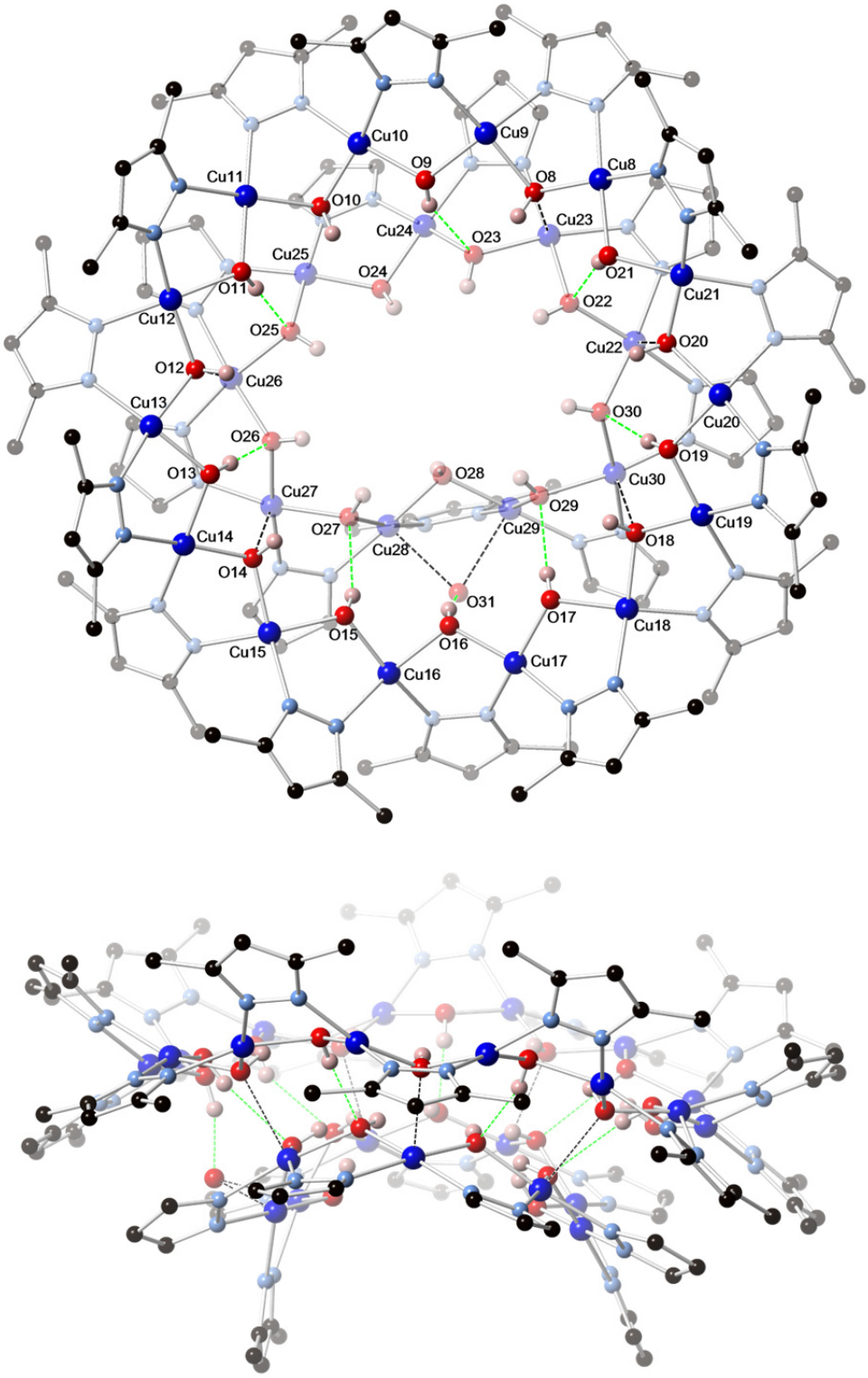

Figure S42. Top- and side-views of the Cu_9- and Cu_{14}-rings in **2**, showing hydrogen-bonding (green dashed lines for O···O distances <3.00(5) Å, grey dashed lines for O···O distances 3.00(5)−3.20(5) Å) and axial Cu-O interactions (black dashed lines for Cu···O distances <2.50 Å) between the two (only the major component of the disordered units is shown).

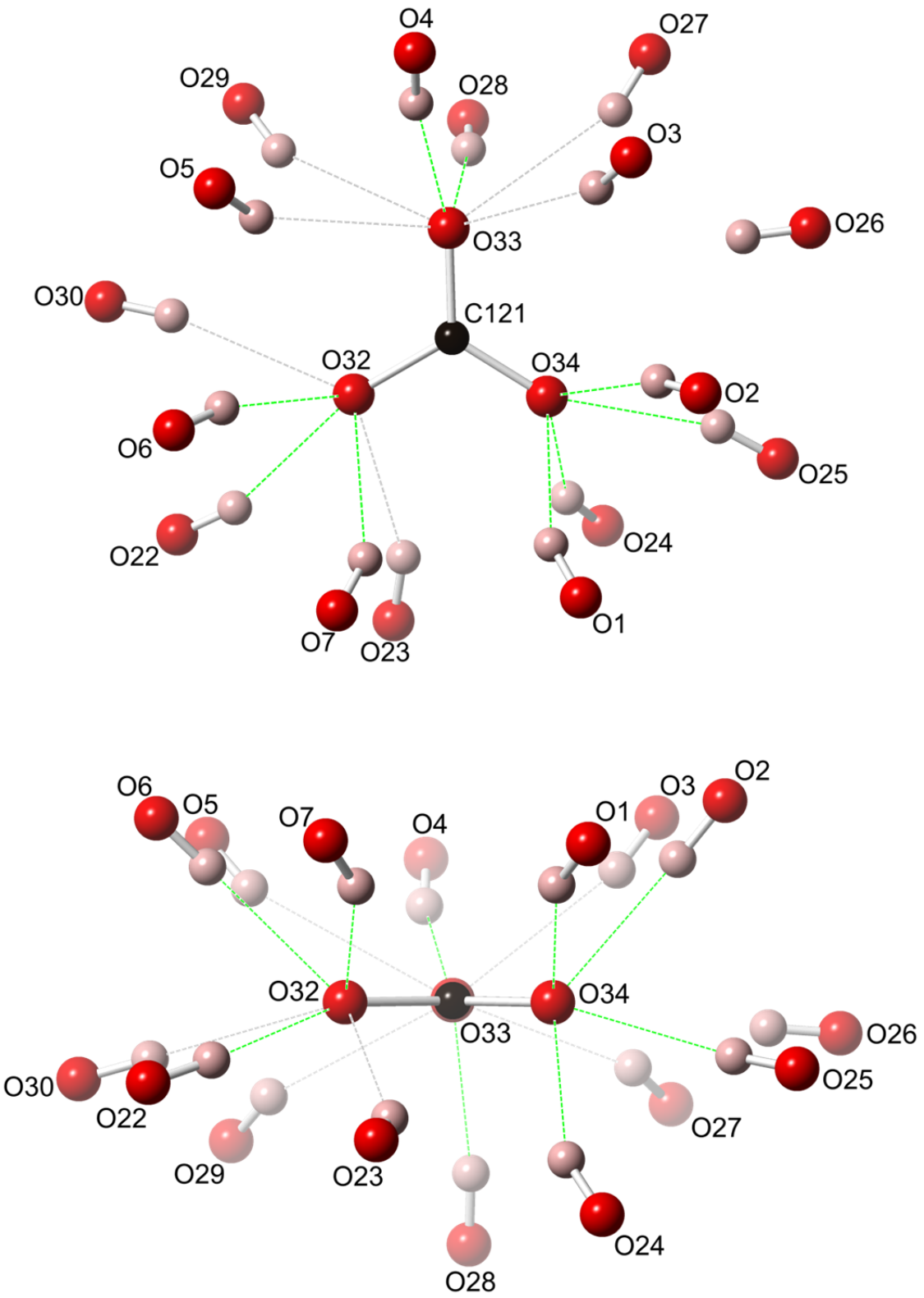

Figure S43. Top- and side-views of the hydrogen-bonding pattern (green dashed lines for O···O distances <3.00(5) Å, grey dashed lines for O···O distances 3.00(5)−3.20(5) Å) to the carbonate ion in **2** (only the major component of the disordered carbonate ion is shown).

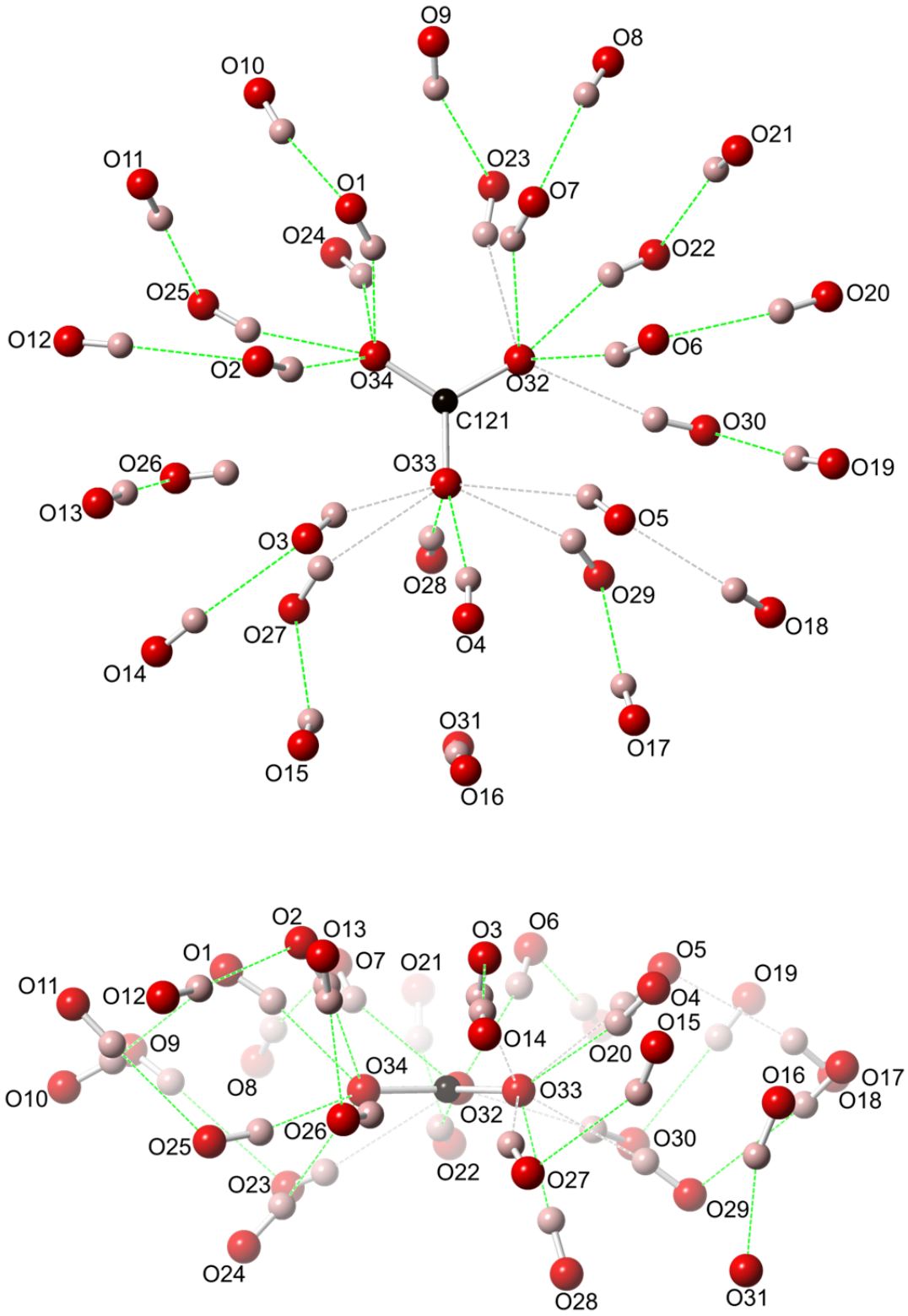

Figure S44. Top- and side-views of the overall hydrogen-bonding pattern (green dashed lines for O···O distances <3.00(5) Å, grey dashed lines for O···O distances 3.00(5)−3.20(5) Å) in **2**, converging at the central carbonate ion (only the major component of the disordered carbonate ion is shown).

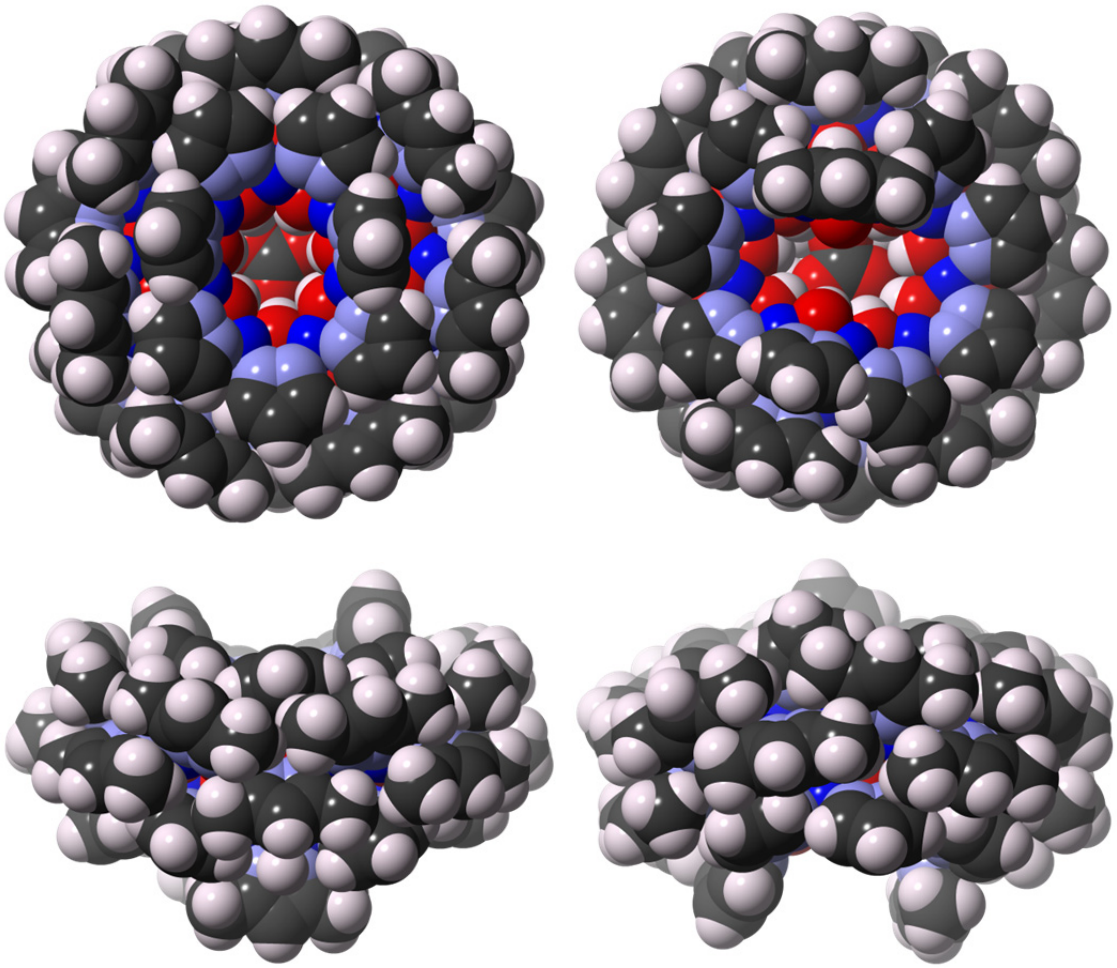

Figure S45. Space-filling representations (two different top- and side-views) of **2** (only the major component of the disordered units is shown).

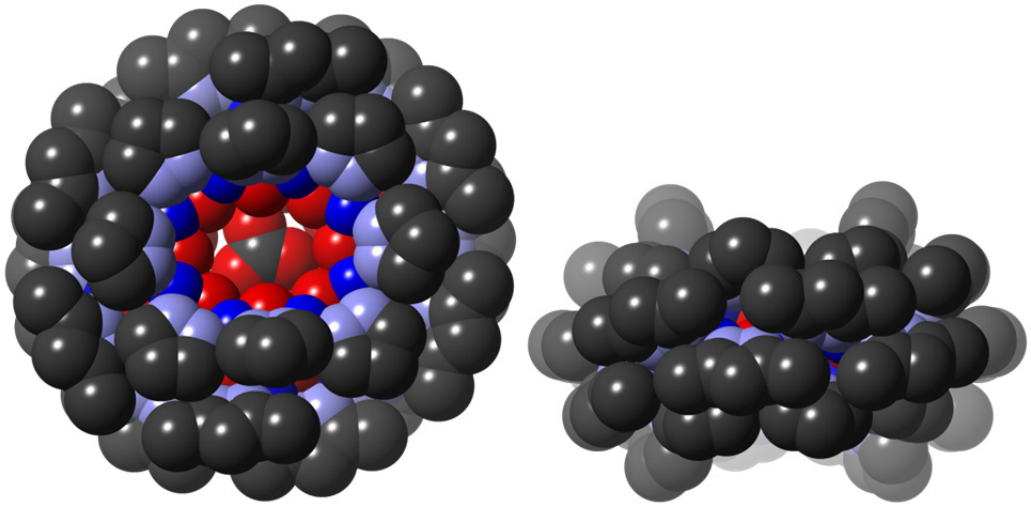

Figure S46. Space-filling representations (top- and side-views) of **3** (no H-atoms and only one position of the disordered CO_3^{2-} ion is shown).

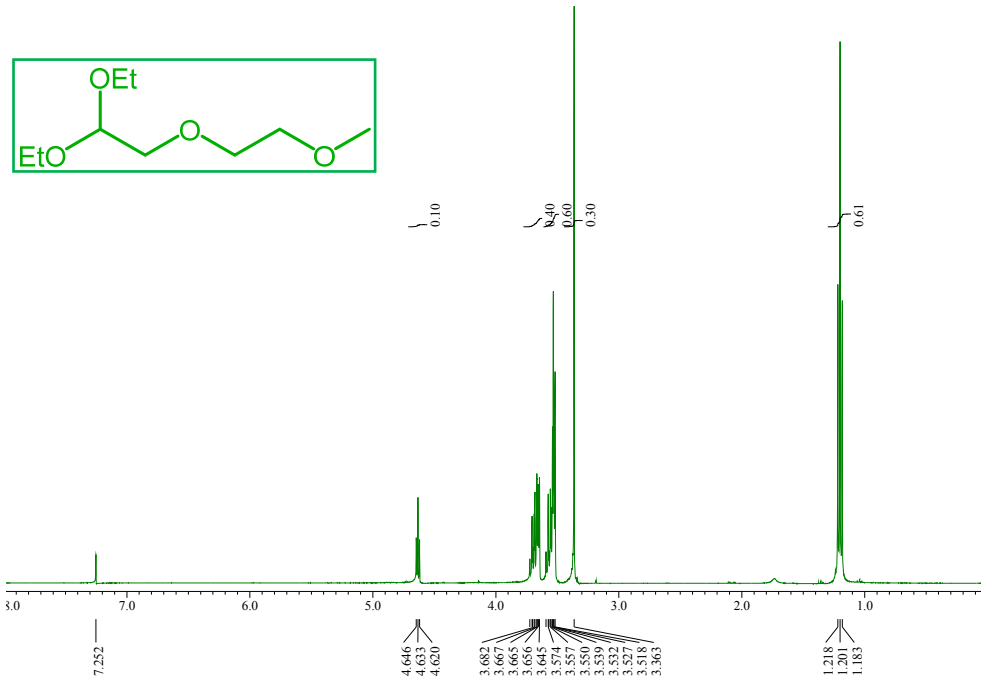

Figure S47. ^{1}H NMR spectrum (400 MHz, $CDCl_3$) of 7-ethoxy-2,5,8-trioxadecane.

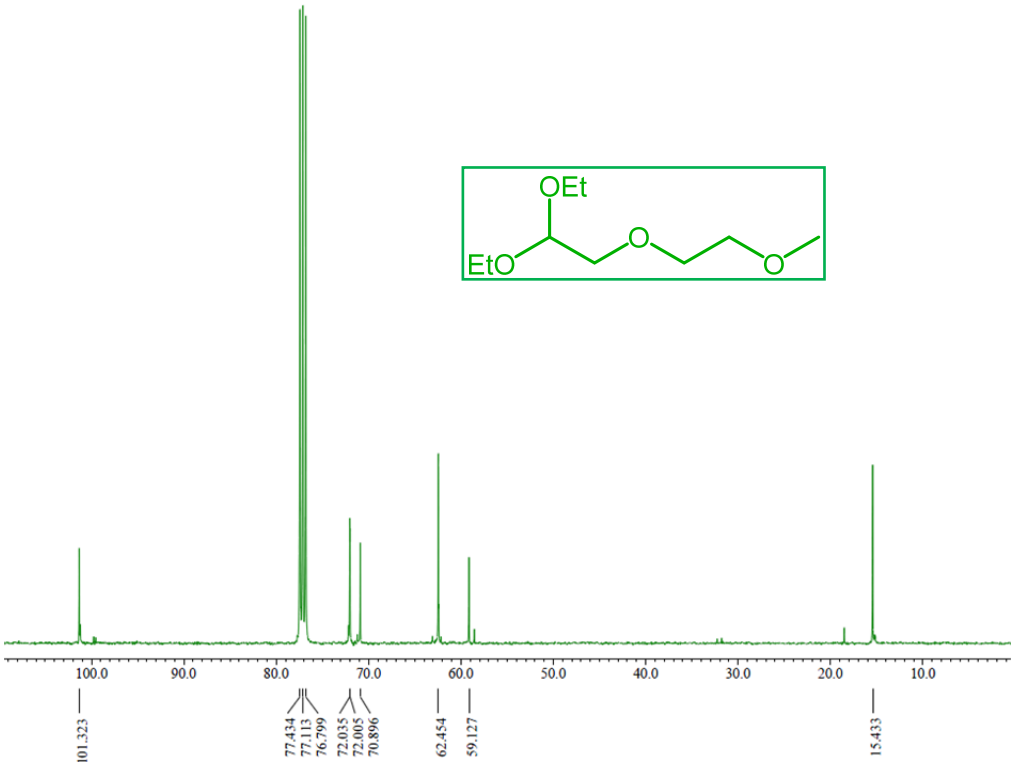

Figure S48. ^{13}C-NMR spectrum (101 MHz, $CDCl_3$) of 7-ethoxy-2,5,8-trioxadecane.

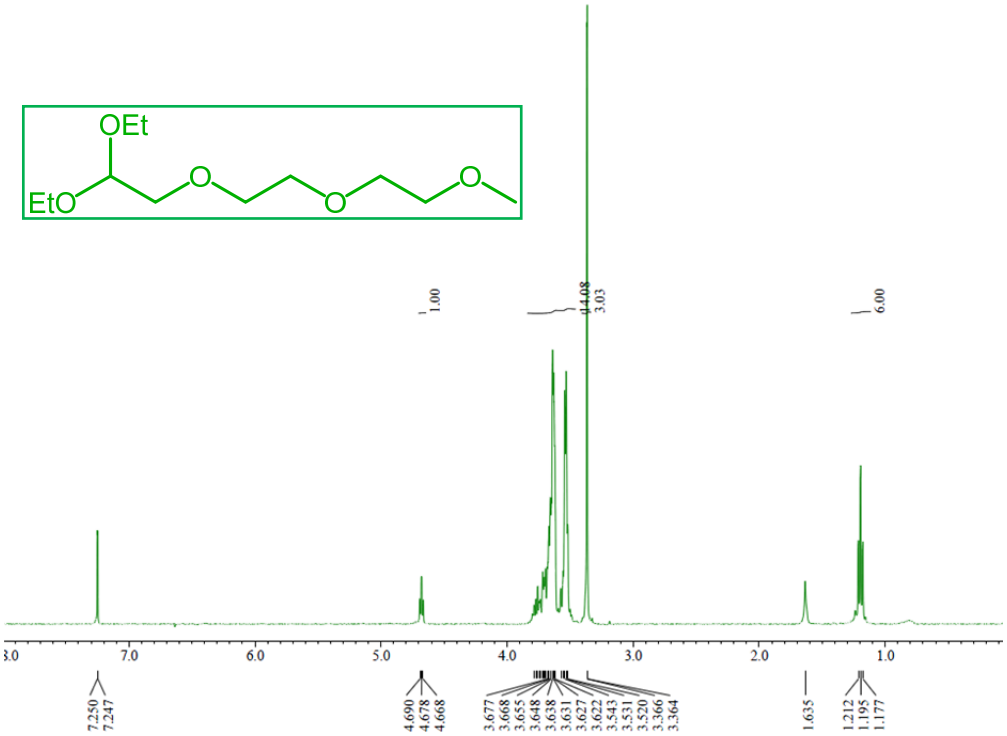

Figure S49. ^{1}H NMR spectrum (400 MHz, $CDCl_3$) of 10-ethoxy-2,5,8,11-tetraoxatridecane.

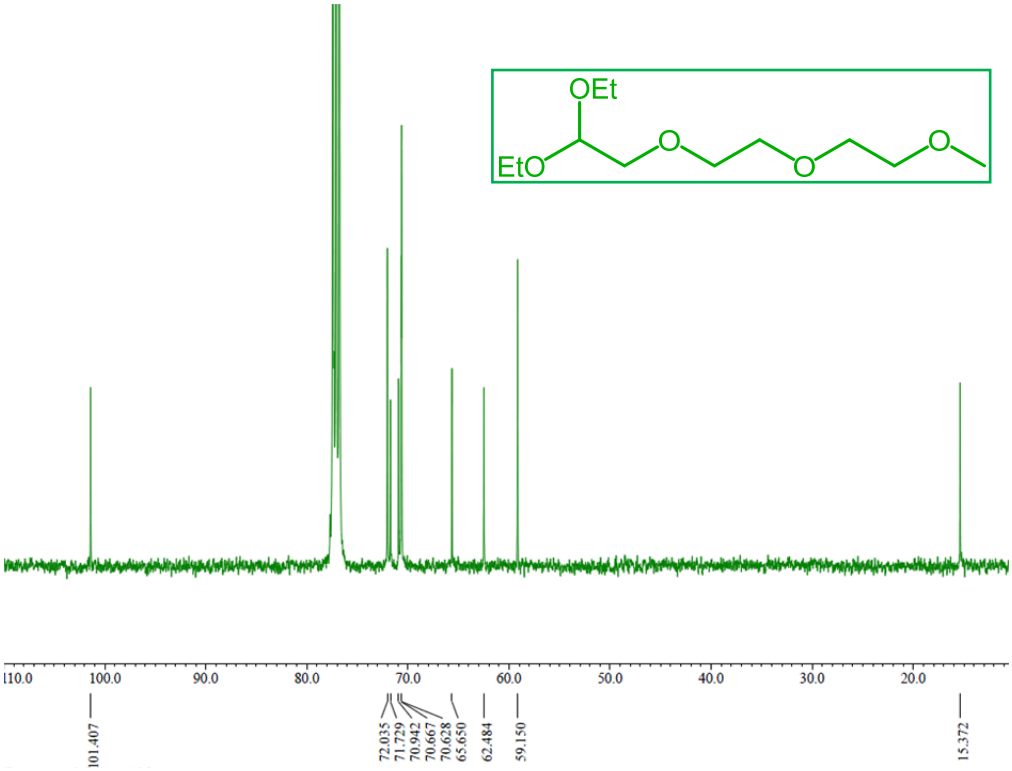

Figure S50. ^{13}C-NMR spectrum (101 MHz, $CDCl_3$) of 10-ethoxy-2,5,8,11-tetraoxatridecane.

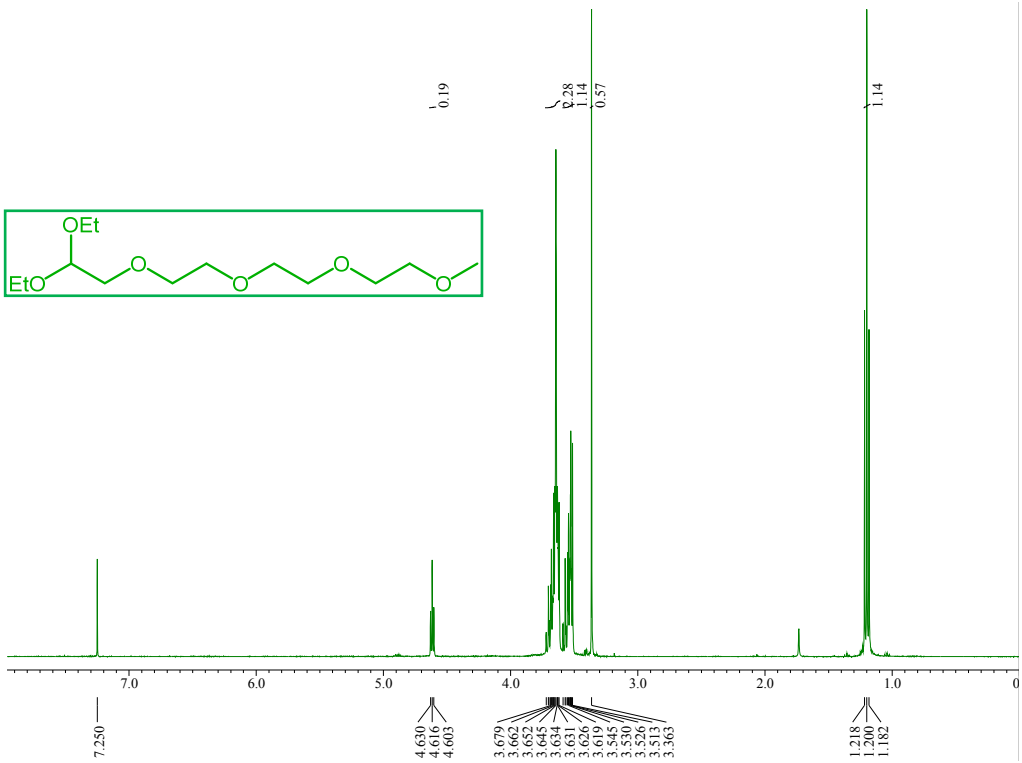

Figure S51. ^{1}H NMR spectrum (400 MHz, $CDCl_3$) of 13-ethoxy-2,5,8,11,14-pentaoxahexadecane.

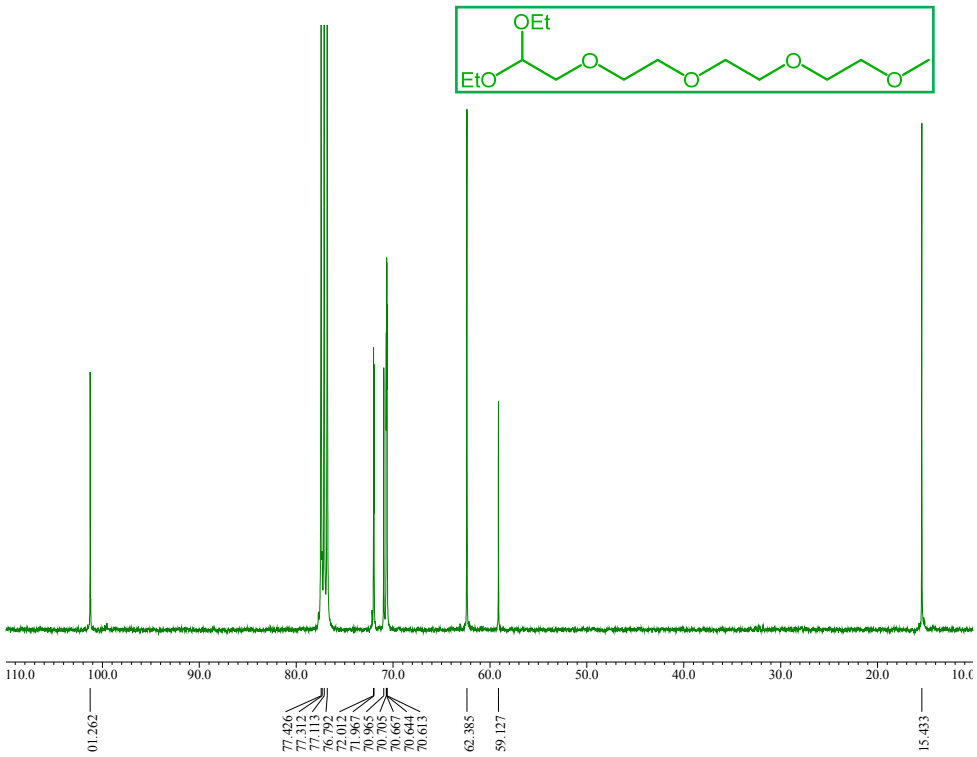

Figure S52. ^{13}C-NMR spectrum (101 MHz, $CDCl_3$) of 13-ethoxy-2,5,8,11,14-pentaoxahexadecane.

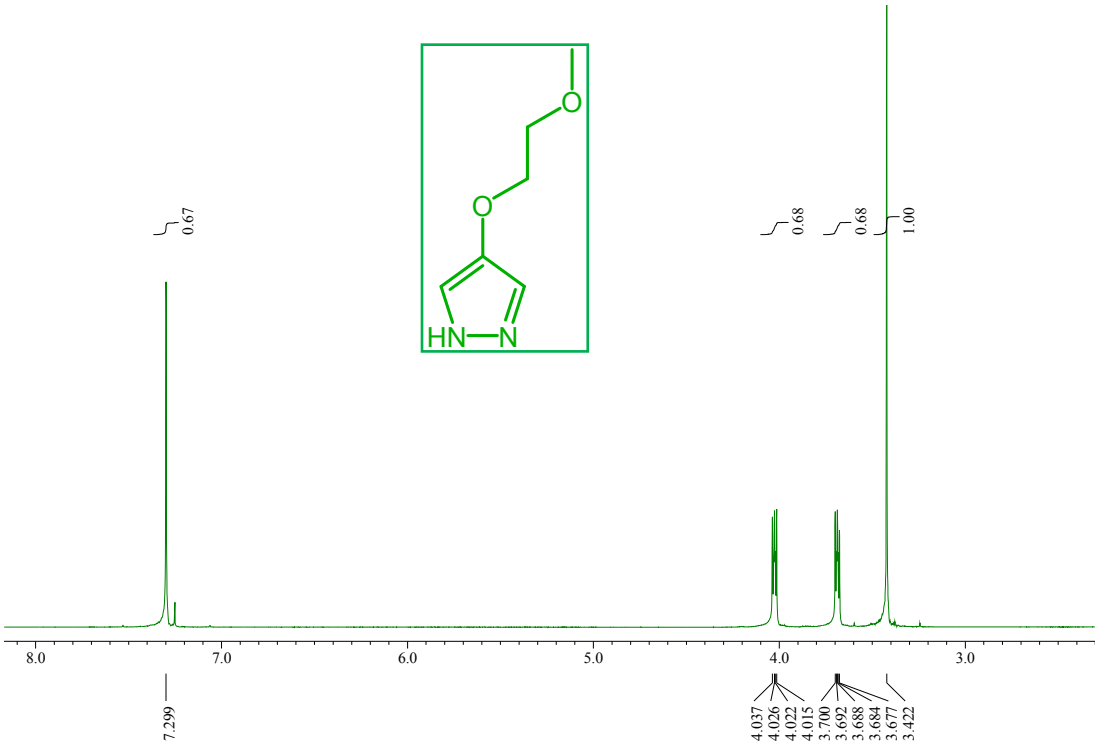

Figure S53. ^{1}H NMR spectrum (400 MHz, $CDCl_3$) of 4-(2-methoxyethoxy)-1*H*-pyrazole.

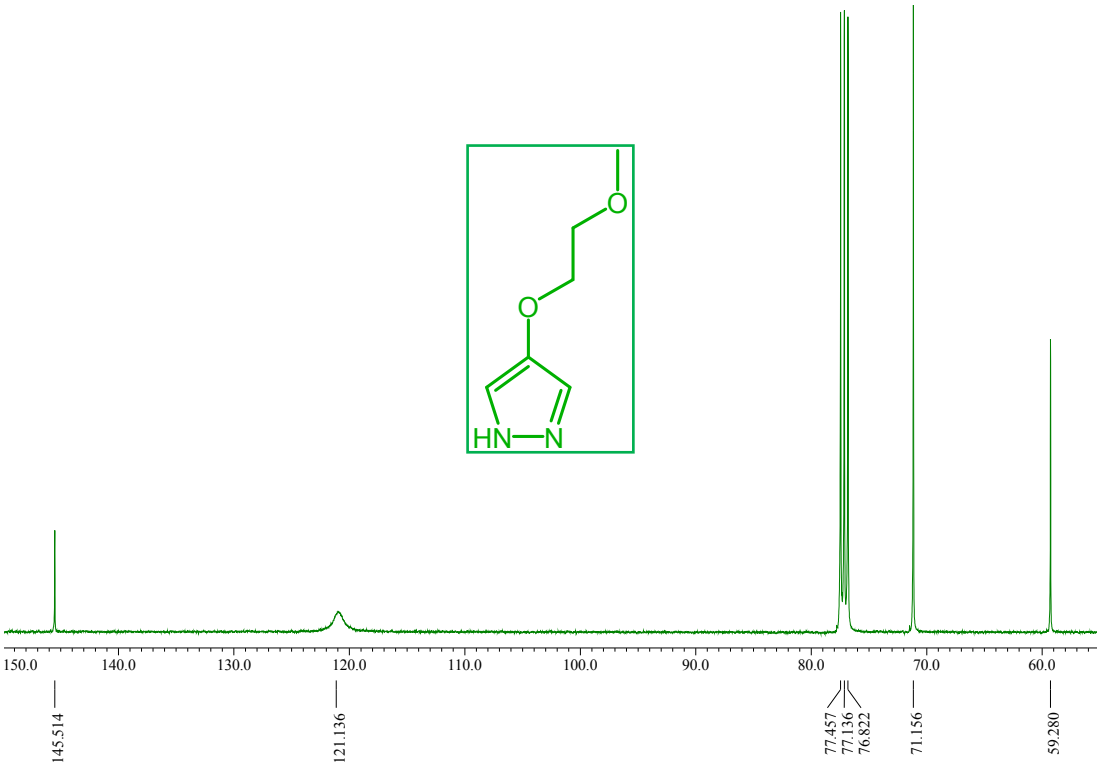

Figure S54. ^{13}C-NMR spectrum (101 MHz, $CDCl_3$) of 4-(2-methoxyethoxy)-1*H*-pyrazole.

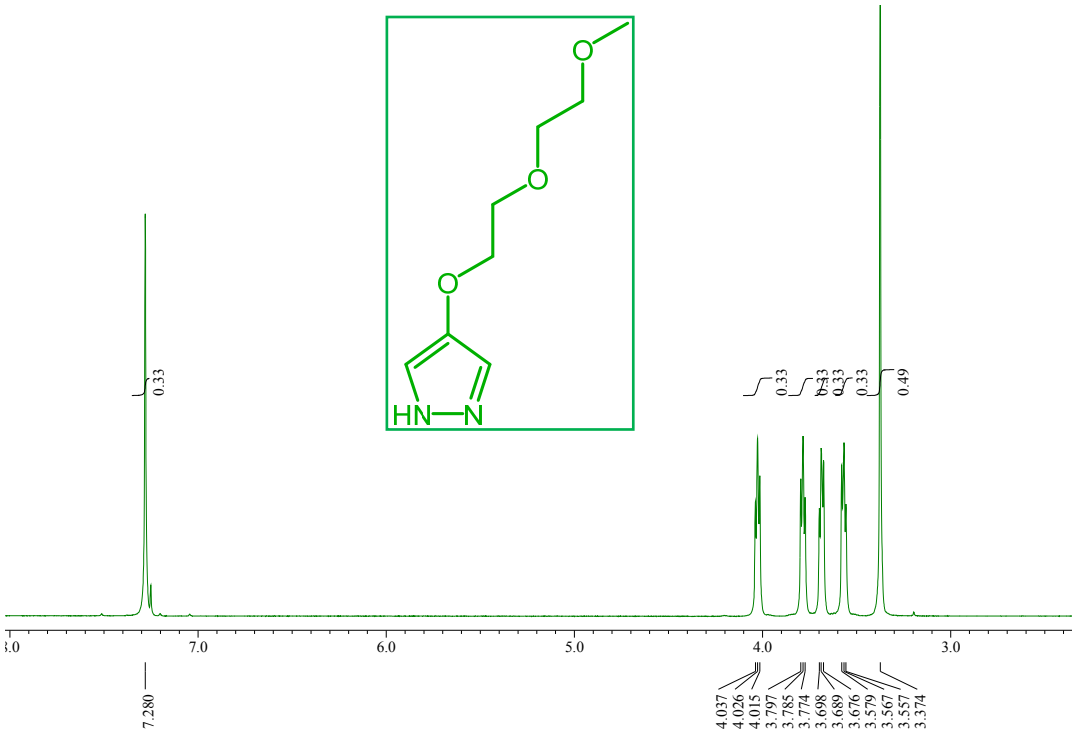

Figure S55. ^{1}H NMR spectrum (400 MHz, $CDCl_3$) of 4-(2-(2-methoxyethoxy)ethoxy)pyrazole.

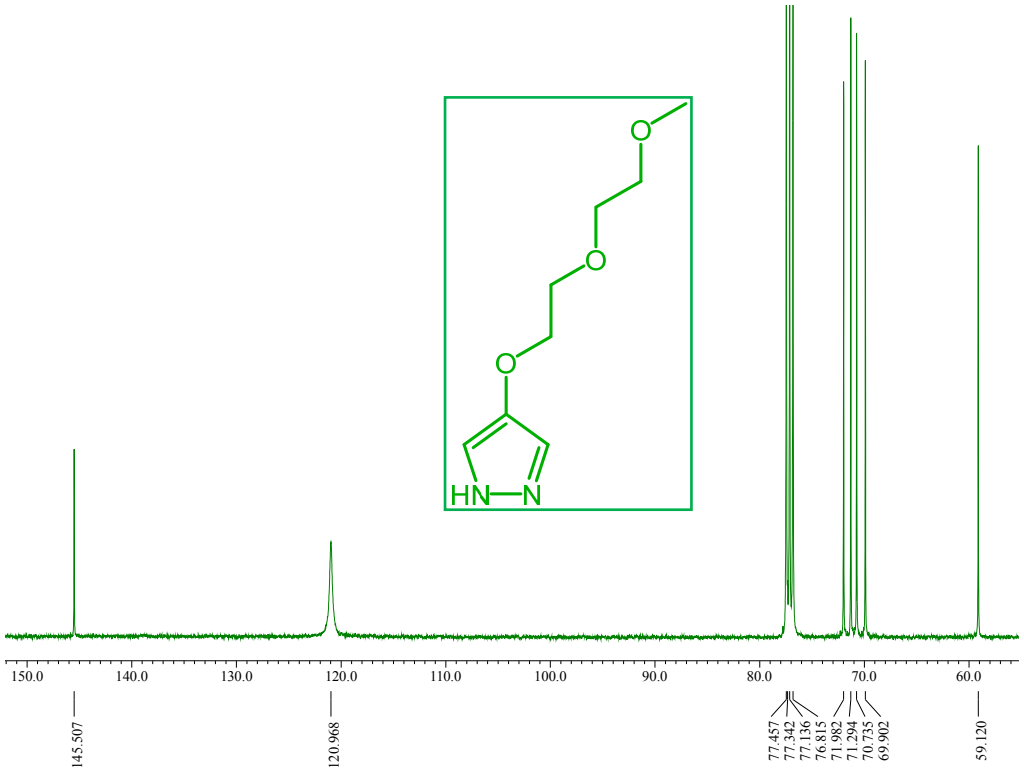

Figure S56. ^{13}C-NMR spectrum (101 MHz, $CDCl_3$) of 4-(2-(2-methoxyethoxy)ethoxy)pyrazole.

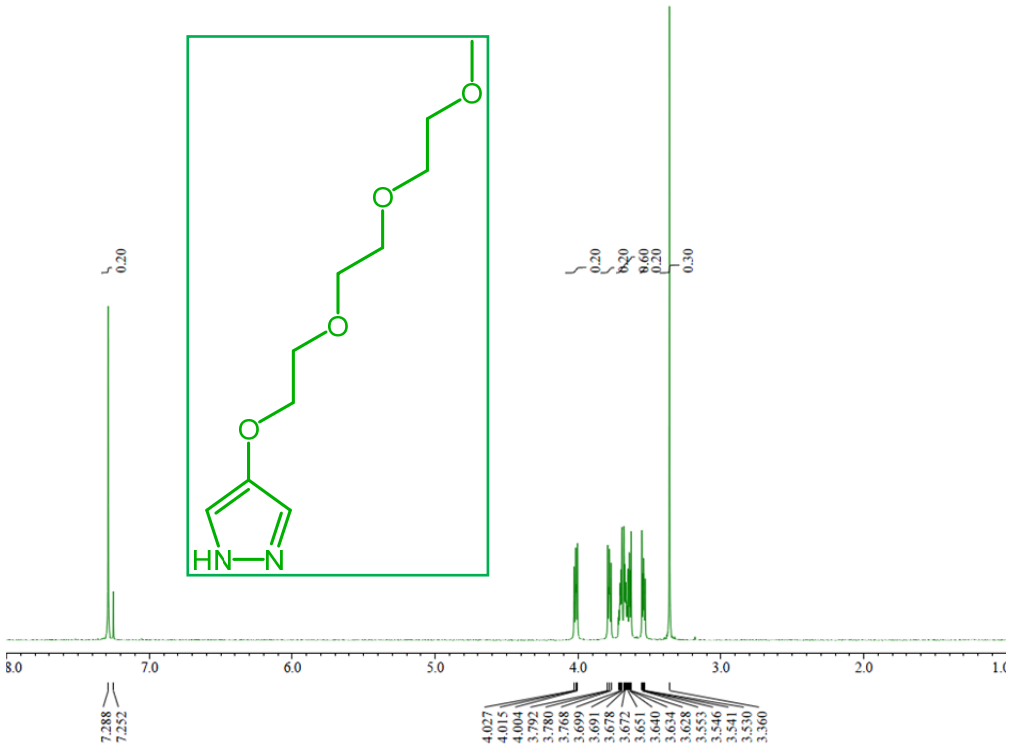

Figure S57. ^{1}H NMR spectrum (400 MHz, $CDCl_3$) of 4-(2-(2-(2-methoxyethoxy)ethoxy)ethoxy)pyrazole.

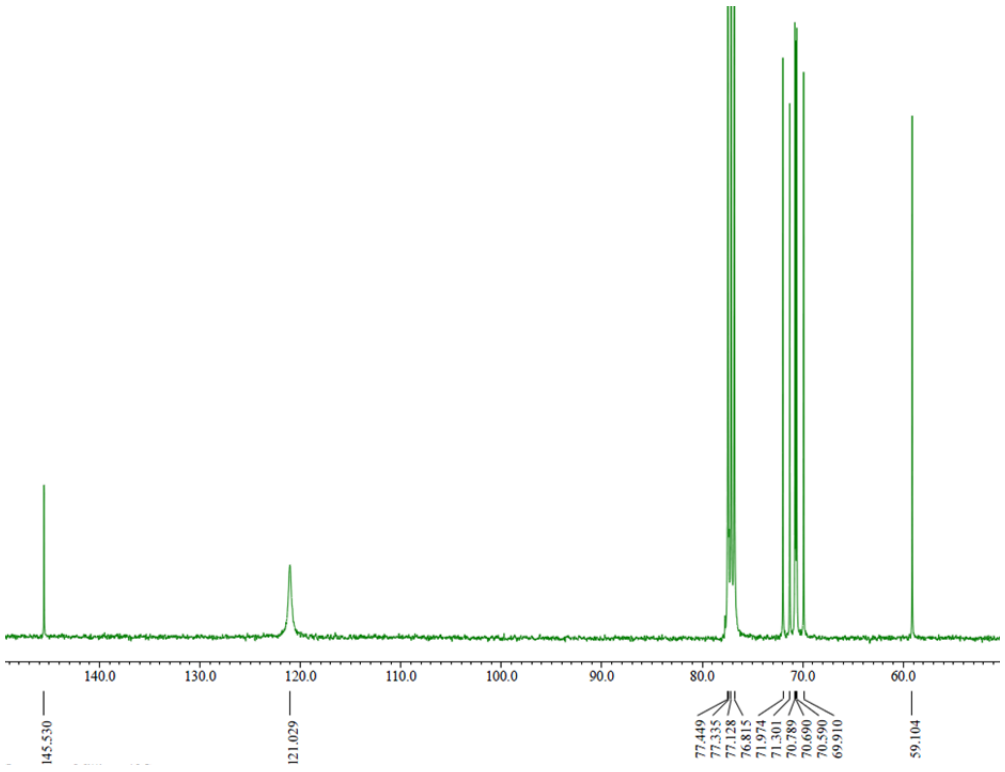

S58. ^{13}C-NMR spectrum (101 MHz, $CDCl_3$) of 4-(2-(2-(2-methoxyethoxy)ethoxy)ethoxy)pyrazole.

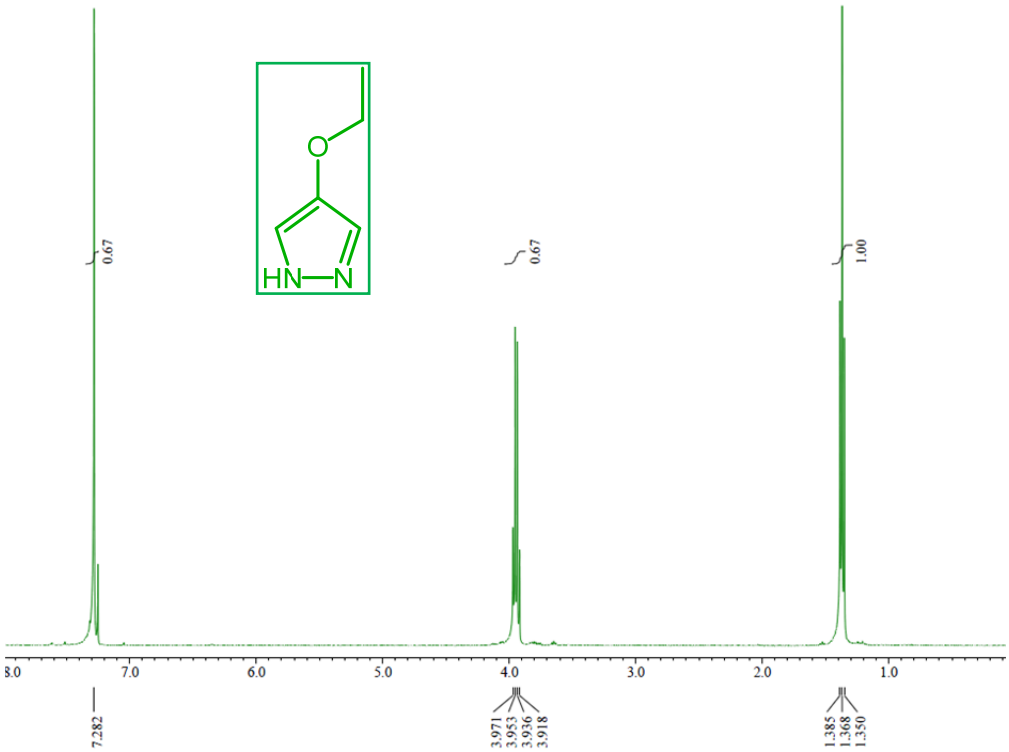

Figure S59. ^{1}H NMR spectrum (400 MHz, $CDCl_3$) of 4-ethoxypyrazole.

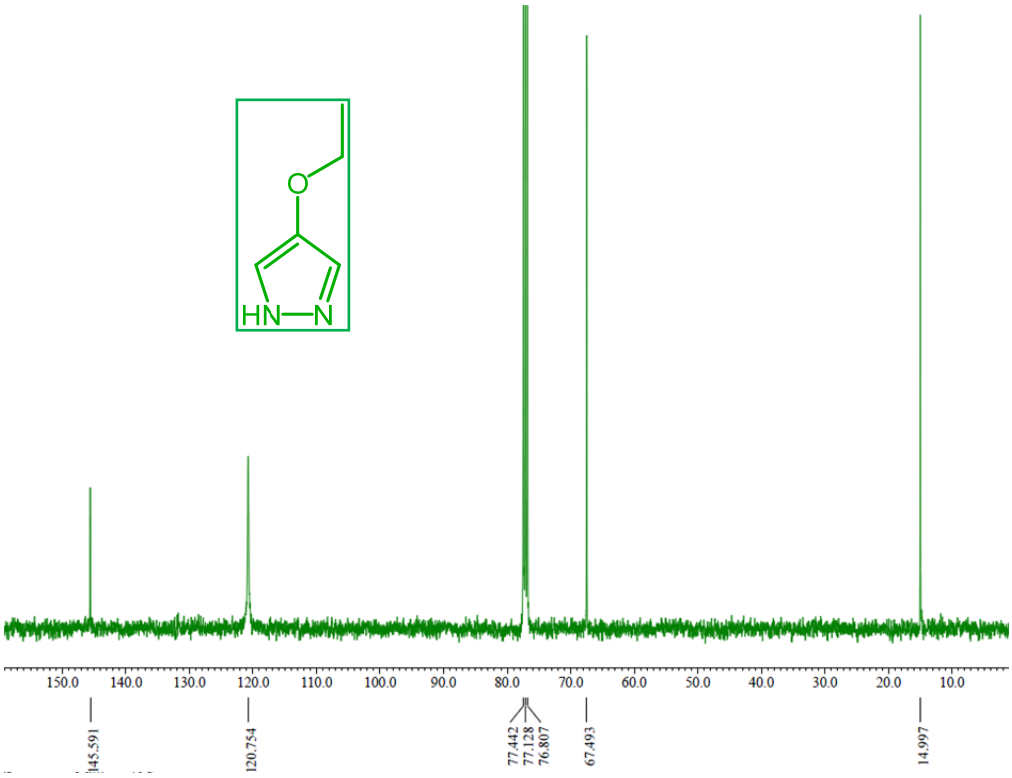

S60. ^{13}C-NMR spectrum (101 MHz, $CDCl_3$) of 4-ethoxypyrazole.

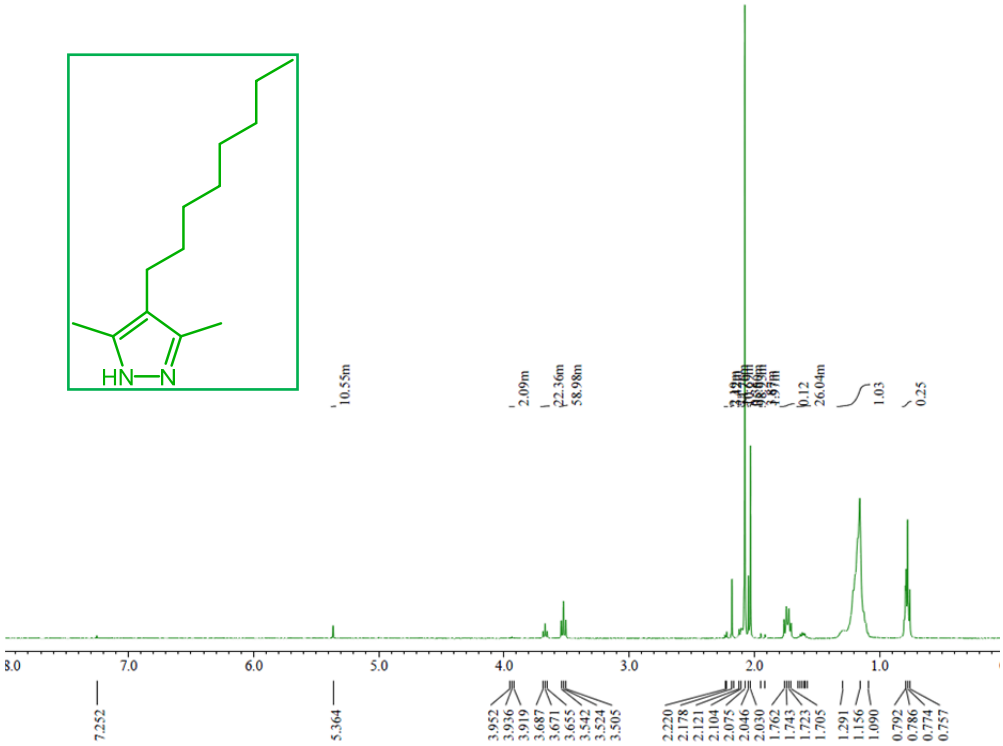

Figure S61. ^{1}H NMR spectrum (400 MHz, $CDCl_3$) of 3,5-dimethyl-4-octylpyrazole.

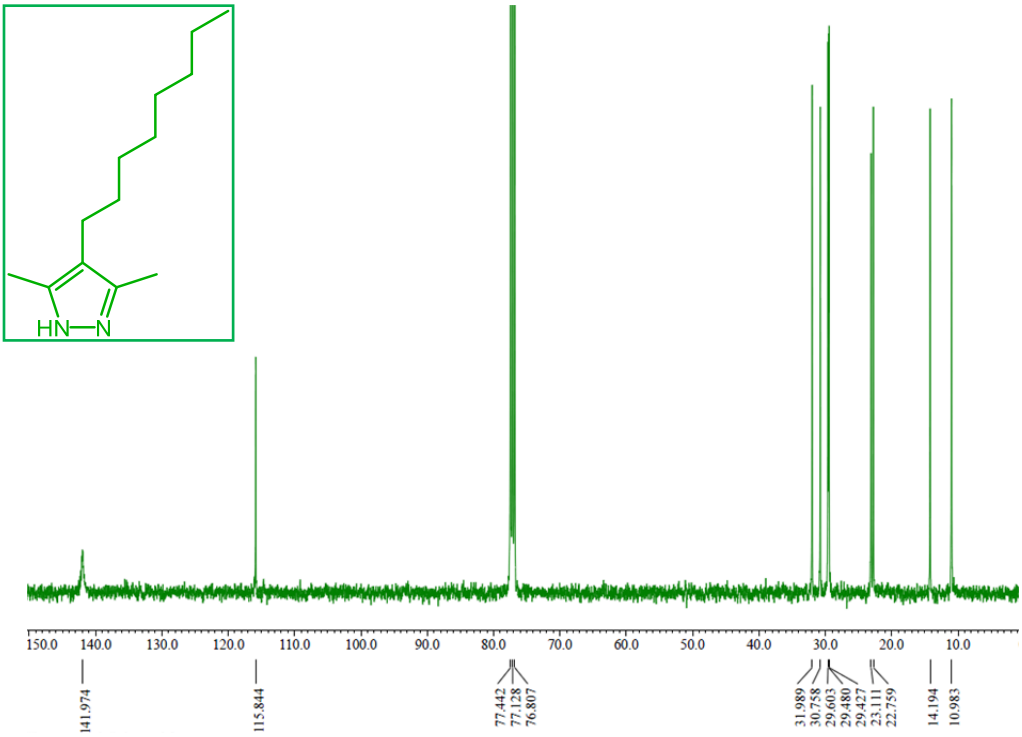

S62. ^{13}C-NMR spectrum (101 MHz, $CDCl_3$) of 3,5-dimethyl-4-octylpyrazole.